University of Stavanger

Faculty of Science and Technology

MASTER'S THESIS

Study program/ Specialization: Petroleum Technology/ Drilling	Spring semester, 2014 Open / Restricted access
Writer: Vegard Dyrseth	…… (Writer's signature)
Faculty supervisor: Thor Martin Svartås External supervisor(s):	
Thesis title: Simulations of the inner heat coefficient during methane hydrate formation and growth in a stirred cell reactor	
Credits (ECTS):	
Key words: Methane Hydrates Growth Simulation Heat Transfer Inner Heat Coefficient	Pages: 75 + enclosure: 9 Stavanger, 16.06.2014 Date/year

Acknowledgments

The writing of this thesis has left me with mixed emotions, as it effectively marks the beginning of the end of my time at the University of Stavanger. Here I have enjoyed many good years with rewarding studies and great classmates where I have learnt to appreciate the great atmosphere the university has to offer. I chose this thesis, knowing very well that it is a very complex field, still with many unknowns, which has become evident throughout the entire process. Nevertheless, it has come to an end and in this chapter, I would like to thank the people who have assisted me and made the efforts worthwhile.

First of all, I would like to thank Thor Martin Svartaas for allowing me the opportunity to write this thesis, and for taking the time for discussions, as well as providing constructive critique and feedback along the way.

I would also like to thank Professor Runar Bøe for providing the simulation model used, as well as offering information and good explanations for all my questions directed his way.

I would like to thank PhD candidate Remi Menindinyo for taking time out of his schedule to show me the experimental procedure, and further my understanding of the hydrate formation process.

I would like to thank my parents, Arild and Reidun Dyrseth, which have been cornerstones throughout my entire education.

Last but not least, I would like to express a special thank you to Nina Frøyland, for helping me keep my hopes and spirit up throughout the demanding task of writing this master thesis.

Summary

In the thesis presented in this paper, simulations have been performed in order to investigate the inner heat coefficient of a hydrate-testing cell as a function of varying stirring rates, initial water amounts, and testing temperatures.

The model used in the simulation is based on heat,-and energy balance, where the inner heat coefficient is estimated as a result of the measured temperatures, and temperature differentials between the inside of the testing cell, and the cooling bath surrounding the cell. The testing conditions were varied in a range from 6-8°C, and 50-100 ml initial water, with stirring rates at 500, 700, and 1200 rpm. For each case, three to four experiments were performed, resulting in comparable data to find any differences. The assumption was that during close to identical test procedures, the values for the inner heat coefficient should remain within certain value-ranges.

The simulations were based on the initial hydrate growth phase, called region 1, which is defined as the domain for first visual hydrate formation, where gas flow increases drastically. The starting point of each simulation was just before the gas flow exceeded 300-400 nml/min to ensure sure that the growth phase had started, and the nucleation phase was finished. The simulation lasted approximately two minutes after the maximum gas flow had been observed.

Each simulation resulted in two plots, where the first consisted of temperatures, and the other showed heat generation from the process, plotted against time-units applied for the simulation. The inner heat coefficient was found by retrofitting the simulated interior temperature, to the corresponding measured temperature. This was performed for 53 cases, where a trend seemed to emerge. As the stirring rate increased, the gas consumption increased, which meant that within the roughly three minute simulation period, the total amount of hydrates formed increased with the stirring rate. The stirring rate seemed to have a dominant effect on the inner heat coefficient, as the lowest hi-values were found for the 1200-rpm case in a majority of the trials. This is contrary to the prevailing hypothesis, where the Reynolds number and turbulence was thought to determine the convection inside the cell, and therefore increase the inner heat coefficient, as stirring rate increased.

Nomenclature

A_i	Inner wall surface (In test cell)
$A_{(g-1)}$	Gas-liquid interface area
A_p	Surface area of each particle
C_i	Specific heat capacity for component i
C_f	Shape factor for homogeneous or heterogeneous nucleation
C_p	Specific heat capacity for constant pressure
C_{wo}	Initial concentration of water
D_a	Diameter of rotating stirring blade
D_T	Diameter of test cell
f^b	Fugacity of component in the bulk liquid
f^{eq}	Equilibrium fugacity of component in the liquid at hydrate interface
$f_{b,j}$	Bulk phase experimental fugacity of component j, at temperature T
$f_{\infty,j}$	Equilibrium fugacity of component j, at temperature T
ΔG	Gibbs free energy
ΔG_s	Surface excess free energy
G_v	Volume excess free energy
Δg_v	Free energy change per unit volume
G_{crit}	Excess free energy where spontaneous growth occurs for homogenous nucleation
G'_{crit}	Excess free energy where spontaneous growth occurs for heterogeneous nucleation
HEN	Heterogeneous nucleation
HON	Homogeneous nucleation
ΔH	Enthalpy
H_i	Initial enthalpy (reactant)
H_f	Final enthalpy (product)
h_i	Inner heat coefficient
h_o	Outer heat coefficient
Δh_H	Heat of hydrate formation per unit mass of hydrate
K	Thermal conductivity for test cell
K^*	Hydrate formation growth rate constant, combining rates for diffusion and adsorption
m_i	Mass of component
$M_{th,i}$	Thermal mass of component
N	Stirring rate

Nml	Normal milliliters
N_G	Molar amount of gas
N_w	Molar amount of water
N_H	Molar amount of hydrate
$\dot{N}_G$	Rate of change in total gas amount
$\dot{N}_R$	Consumed gas rate
$\dot{N}_w$	Consumed water rate in hydrate formation
$\dot{N}_H$	Hydrate growth rate
n_w	Number of water molecules per gas molecule
P	Pressure
P^{∞}	Equilibrium pressure
Pr	Prandtls number
$\dot{q}_i$	Sensible heat increase
$\dot{q}_{conv}$	Convection at inner border
$\dot{q}_R$	Heat of reaction
r	Radius of solid particle
r_c	Critical radius where spontaneous growth occurs
R	Gas constant
Re	Reynolds number
RPM	Rotations per minute
ΔS	Entropy
sI	Hydrate structure I
sII	Hydrate structure II
sH	Hydrate structure H
$\left.\frac{\partial T}{\partial x}\right\|_{x=x_{h-}}$	Temperature gradient on the hydrate side of the interface
$\left.\frac{\partial T}{\partial x}\right\|_{x=x_{h+}}$	Temperature gradient on the water side of the interface
$\left.\frac{\partial T}{\partial t}\right\|_{i}$	Inner temperature gradient for test cell
T_i	Interior cell temperature
T_b	Cooling bath temperature
T_o	Exterior cell temperature
$(T_i - T_0)$	Temperature difference across the wall
V_g	Volume of gas
V_h	Volume of hydrate building units
W	Work

z	Compressibility factor
δ	Hydrate film thickness
λ_i	Thermal conductivity for component i
σ	Surface tension
σ_{ef}	Effective specific surface energy
ρ	Density
μ	Viscosity
$\Delta\mu$	Supersaturation
v_i	Molar volume of component i
v_f	Lateral hydrate film growth rate
x_{int}	Bulk liquid mole fraction
θ_j	Fractional filling of hydrate cages by free water
Φ	Fraction used to convert G_{crit} to G'_{crit}

List of figures

List of tables

Table of contents

1 Introduction

1.1 A general overview

Gas hydrates are naturally occurring ice-like crystalline solids that can form in the presence of gas and water during the right circumstances. That is to say, during high pressures and low temperatures-typically in the region 20 to 23°C (personal communication with T.M. Svartås, 2014), dependent of gas composition and pressure. Gas molecules (guests) are trapped inside water cavities (hosts) that are composed of hydrogen-bonded water molecules kept together by van der Waal forces. Most common of the guest molecules are methane, ethane, propane and carbon dioxide.(Sloan and Koh 2008)

Hydrates can take many geometric forms, often determined by which types of gasses that inhabit the cavities. The structural form, or crystalline lattice, is not a stable form on its own due to the repulsive forces between the lattices, but the encaged gas serves as a stabilizing agent. From a visual perspective, hydrates share a similar appearance as ice, but the properties of the hydrates are very different. Hydrates may form at temperatures well above the freezing point for water, if the pressure is sufficiently high.(Sloan and Koh 2008)

In earlier years, hydrates were considered a curiosity more than a nuisance, as they were discovered already in 1810 in experiments conducted by Davy (Davy, 1811), where he observed that a solution of chlorine in gas froze more readily than pure water. It was not until Hammerschmidt in the mid-1930's (Hammerschmidt, 1934) determined that hydrates were blocking production pipelines that the field of research intensified. Hydrates forming in oil pipelines in today's industry can be a very big concern, as melting them following their initial formation, is a cumbersome and tedious process. Interests lie in finding methods to prohibit hydrate growth by inhibitors or regulating temperature and pressure, and ways to detect hydrate growth in the pipelines at an early stage in order to execute countermeasures.(Sloan and Koh 2008)

However, the interest in hydrates are not exclusively in finding ways to prevent them, as vast amounts of potentially commercial natural gas are trapped inside hydrates in permafrost regions, and subsea in deep waters. Even though estimation of the magnitude is difficult, it is clear that the hydrate gas reserves could be significant. It is however, difficult to extract this resource, as the locations often prove challenging. (Sloan and Koh 2008)

Extensive research has been completed on hydrates, yet all aspects are not fully understood. Especially as regards at what conditions hydrates form (nucleation) and their growth kinetics. Multiple models have been proposed, where some are mentioned in chapter three, based on heat transfer(Uchida, Ebinuma et al. 1999, Freer, Sami Selim et al. 2001, Mori 2001, Mochizuki and Mori 2006) and mass consumption/transfer(Skovborg and Rasmussen 1994). In addition, an intrinsic kinetic growth model (Englezos, Kalogerakis et al. 1987), which serves as a basis for many of the later models.

Hydrate forming is an exothermic process, which allows for heat measurements due to increased temperature to the surroundings. In a closed environment, as is usually the case during lab trials, one can also measure the amount of gas consumed during the process. Along with the measured heat loss, it is possible to measure the amount of hydrate formed per time-unit. Furthermore, one can calculate the amount of energy released (enthalpy) per time-unit. These variables are at the center of several of the different hydrate-related models developed.(Sloan and Koh 2008)

1.2 Definition of thesis

In order to properly define the heat transport which takes place during hydrate growth, it is crucial with good models/descriptions, with proper assumptions, and reliable experimental equipment. As mentioned earlier, hydrate growth is an exothermic process, which means that it releases energy in the form of heat. In this thesis, the focus will be on an approximate constant temperature situation during the growth phase, which is achieved by using a cooling system, designed to keep constant temperature in the medium outside the reactor. Any excess heat will be removed by convection in water and conduction through the test cell wall, and

when energy production by hydrate formation is run at constant rate, the heat balance between the interior and exterior of the cell reactor will approach a steady state. (personal communication with T.M. Svartås, 2014).

During the experiments it is possible to measure energy created by the process as a function of balanced temperature increase/heat loss, measuring the consumed quantity of gas entering the system. The amount of gas consumed per time unit is directly related to the energy release via the heat of formation. This enables the calculation of the amount of hydrates created per time-unit. Furthermore, it is possible to calculate the amount of energy released, or enthalpy, per time-unit if the heat of formation is known for the hydrate formed. This energy dissipates and is lost to its surroundings, the cell walls and the cooling water. The temperature inside the test cell will, after it has reached steady-state, appear to remain constant because any excess heat is transported out of the test cell. If the enthalpy of formation is known, the amount of energy released can be compared to the amount of hydrates formed. In order to do this it is important with applicable models and a good description of the heat transfer properties of the system. In the present MSc thesis, the goal is to examine a model created by Professor Runar Bøe (UiS), and to look at the general fit between simulated and measured values for the interior temperature of the cell, along with the simulated heat generation of hydrate formation. With these data, it is possible to simulate a value-range for the inner heat coefficient under certain experimental conditions. In an attempt to eliminate effects of the increasing amounts of hydrate in the cell during the growth process, the present work is focused around an early growth stage where the hydrate content in the cell is relatively low (personal communication with R. Bøe, 2014).

The data used for simulations is collected from master candidate Therese Nordbø (2013) experimental trials, and the simulation model, which will be used, is designed by Professor Runar Bøe.

2 Theory

2.1 Geometric structures

Water molecules and small gas molecules, called guests, form gas hydrates. A hydrate looks very similar to that of ice, slush or snow, but is in fact very different. Where ice can form from only pure water, the hydrate needs a guest,-or gas molecule in order to form.

There are three typical structures currently know, from which hydrates usually form, with some exceptions. They consist of structures I, II and H. Classification of structures are determined by the layout of the water molecules and to some extent, the guest molecule entrapped in the cavities

Between the late 1940s and early 1950s , von Stackelberg and coworkers released a summary of two decades worth of work (1954a, 1954b). This work contained a series of x-ray crystal diffraction experiments, which lead to the determination of the two structures, I (sI) and II (sII). (Sloan and Koh 2008)

The structural form of H, was discovered somewhat later by the work of Ripmeester et al. (1987) using Nuclear magnetic ressonance. Jeffrey (1984) listed seven hydrate structures, I-VII, however of these, only sI and sII have been found with hydrocarbon guest molecules. He did not list the structure, H, among these. Structures III-VII mapped by Jeffrey, are considered high-pressure hydrates containing non-natural gases, which make them irrelevant to this particular study.

As hydrates form the water molecules tend to prefer a tetrahedral bond, with angles of 109. 5 degrees. This is, as suggested by Stillinger (1980), the best way of packing molecules because it allows fully developed hydrogens bonds. This in turn creates close to no geometrical distortion, providing the most stable form. (Sloan and Koh 2008)

2.1.1 Cavities in hydrates

A cavity is the open space created by the bonded molecules around it, or so called lattice structure. With respect to hydrates, certain configurations stand out as the building blocks. When describing the configuration of a cavity, a certain nomenclature is used. This particular nomenclature, created by Jeffrey (1984), describes the different polyhedral by using n_i^{mi}. The ni denotes the number of edges in face type "i", whilst *mi* is the number of faces with *ni* edges.

Take the pentagonal dodecahedron as an example. This configuration is found as the small cavity in all hydrate structures. The pentagonal dodecahedron is labeled 5^{12} because it has 12 pentagonal faces with equal edge lengths, and the 5 is denoted because of the pentagon's 5 edges.

The 14-sided cavity, tetrakaidecahedron, is denoted $5^{12}6^2$ because it has 12 pentagonal and 2 hexagonal faces. This configuration serves as the large cavity in sI.

The 16-hedron, hexakaidecahedral, cavity is denoted $5^{12}6^4$ because in addition to the 12 pentagonal faces, it houses in addition 4 hexagonal faces. This configuration is usually found in the large cavities in sII.

The irregular dodecahedron cavity is denoted $4^3 5^6 6^3$ due to its 3 square, 6 pentagonal,-and 3 hexagonal faces. This configuration is usually found as the medium sized cavity in sH.

The largest cavity of the ones presented here, is the icosahedron, which is denoted by $5^{12}6^8$. The structure has 12 pentagonal,-and 8 hexagonal faces and serves as the largest cavity in sH.

To determine the suitable size for a guest molecule in a specific structure, Davidson suggested subtracting the van der Waals radius of the water molecule from the "average cage radius" collected from the approximate radius of the different cage configurations. To determine the upper and lower boundaries for a suitable guest molecule, it is instructive to consider the diameter ratios for a single compound, or hydrate former. The lower boundary is given as 0.76 of the average cavity diameter, whilst the upper boundary is 1.0. If a guest is below 0.76

it is not sufficiently large to stabilize the structure. On the other hand, if the value of 1.0 is surpassed, the cavity will stretch and create strains.

That is to say, any given structural type is dependent on the hydrate former and its size. Either pure gas, or a gas mixture during a given pressure and temperature to create a particular structure. The small cavities of structures sI, sII and sH are all the same, meaning that the different structures may house many of the same components. It is known that the small guests such as Ar, Kr, N_2 and O_2 form sII over sI, but the determination of the structural type is predominantly decided by which gas component/hydrate former that houses the large cavity. The large hydrate formers are unique for each structure (Sloan and Koh 2008).

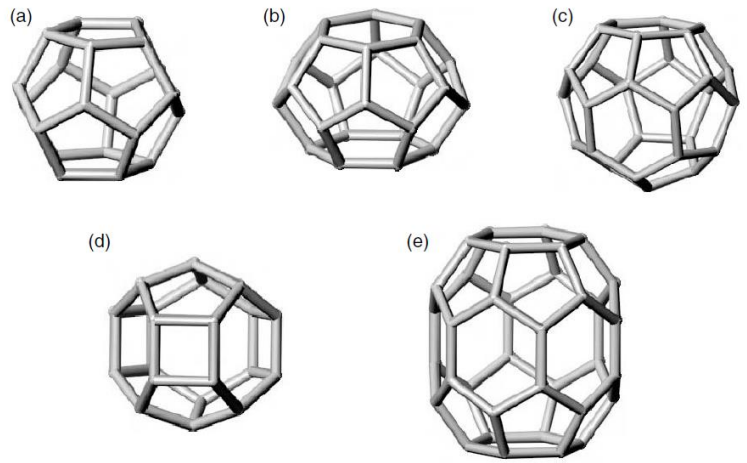

Figure 1 Cavities in gas clathrate hydrates : a) pentagonal dodecahedron (5^{12}), b) tetrakaidecahedron ($5^{12}6^2$), c) hexakaidecahedron ($5^{12}6^4$), d) irregular dodecahedron ($4^3 5^6 6^3$), e) icosahedron ($5^{12}6^8$) (Sloan and Koh 2008)

2.1.2 Structure I

The simplest type of structural form a hydrate can take is sI, which is a cubical shape. This structure consists of the cavity structures, 5^{12} and $5^{12}6^2$. The small cavity is the dodecahedron (5^{12}) which contains 20 water molecules and has a radius of 3.95 Å. Guest molecules usually present include Xe, CH_4, H_2S and more non-polar gas molecules given normal temperature and pressure conditions. The large cavity is a tetrakaidecahedron ($5^{12}6^2$) which consists of 24 water molecules and has a radius of 4.33 Å. With respect to guest molecules, the large cavity

may contain CH_4 and/or C_2H_6. Methane can occupy both the small and the large cavity, whilst ethane can only occupy the large cavity.

Structure I is comprised of six large cavities and two small cavities with 46 water molecules arranged as lattices around the cavities. A trademark of sI is that it will not form if the guest molecules are larger than propane. The present work comprises studies on pure structure I methane hydrate to simplify the system and avoid effects of additional hydrate forming components on essential properties of the hydrate (e.g. enthalpy of formation, equilibrium conditions, etc.)

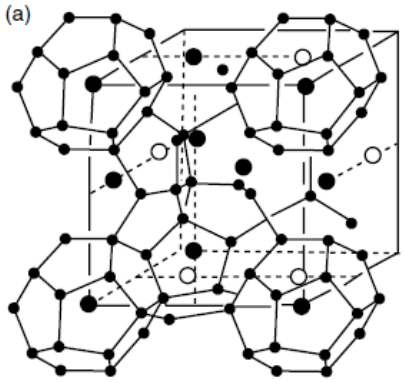

Figure 2 Hydrate crystal unit for sI (McMullan and Jeffrey, 1965)

2.1.3 Structure II

The most common by far in the oil and gas industry, is structure II. It takes on a cubical shape, but unlike structure I, this form is far more complex. It is comprised of small and large cavities. The small cavity is the same as in both sI and sH, which is 5^{12}, or the dodecahedron (more detail in section 2.1.1.) This small cavity only differs from the 5^{12} in sI by having a slightly smaller average radius (3.91 Å.) This could be a reason why pure nitrogen, N_2, forms sII instead of sI, seeing that it would stabilize the cavity better. The large cavity is denoted $5^{12}6^4$, and is called hexakaidecahedron. This cavity is larger than its equivalent in structure I, and can therefore host different and larger guest molecules up to 6.6 Å. Which include propane and iso-butane, ranging from 6.28 to 6.5 in diameter respectively.

The total amount of cavities in sII is 24, consisting of 16 small and 8 large. Even though the average radius of the dodecahedron is smaller in sII, the amount of water molecules per cavity is the same. There are 136 water molecules creating lattices around the 24 cavities.

2.1.4 Structure H

The structural form of H is the least occurring hydrate of the three mentioned. As previously mentioned, it was not part of the list Jeffrey proposed of the seven hydrates and was discovered by Ripmeester as late as 1987. It is proposed that this was the first hydrate prepared, but never recognized, by de Forcrand in 1883, almost one hundred years before its original discovery.

The structure H is a hexagonal shape, which the H denotes. It has small, medium and large cavities and unlike the previous structures, it requires two guest molecules to stabilize. One small/medium sized gas to stabilize the small and medium sized cavities, and one large guest to stabilize the large cavity, whereas the two former can be formed from pure components.

The small cavity is the dodecahedron, 5^{12}, and the medium cavity is the irregular dodecahedron, $4^3 5^6 6^3$. The large cavity is called icosahedron and is denoted by $5^{12}6^8$. This large cavity has a radius of 5.79 Å, accommodating quite large guest molecules. These guest molecules may be 2-methylbutane, 2.2-dimethylbutane, 2.3-dimethylbutane, 2.2.3-trimethylbutane and cyclooctane to name a few. These are not typically found in natural gas, which may explain why sH is scarce to find in oil & gas pipelines. (Sloan and Koh 2008)

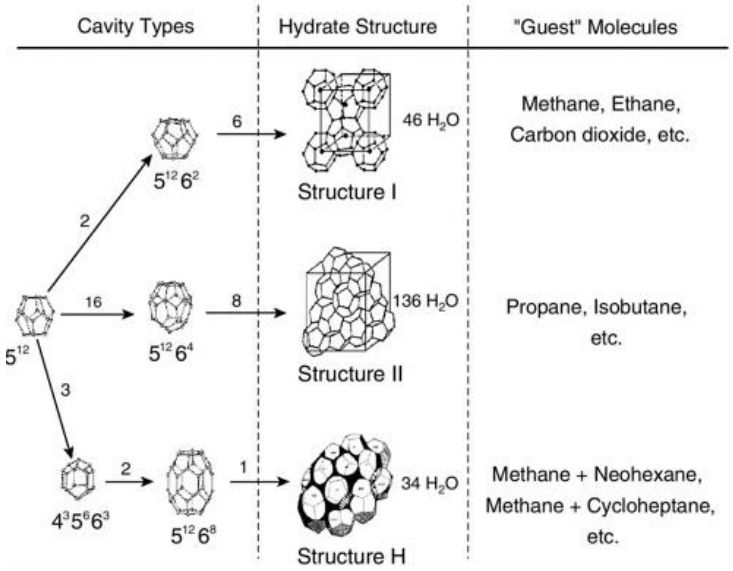

Figure 3 Comparison of hydrate structures,(2004)

2.2 Nucleation

Perhaps the most challenging and intriguing area regarding hydrates, concern how hydrates form, dissociate, and are inhibited with time. Hydrates nucleation is considered a stochastic process, which makes the phenomenon very difficult to observe at actual nucleation point, as well as predicting growth rate. The difference between stochastic and deterministic behavior is illustrated by Figure 4. As an example, it is possible to consider an equilibrium state, where the chance of observing a certain temperature is one, which in turn makes for a deterministic observation. In other words, a certainty. However, for some properties the distribution is along multiple values. It is reasonable to assume that the observed value will be at the peak of the curve, but not a certainty. This is stochastic. With respect to hydrates, it is important to look at the driving forces of the reaction. Hydrates tend to prefer low temperature and high-pressure scenarios. At low driving forces, the values observed are highly stochastic with no clear observable peak. However, at high driving forces, the distribution is much narrower making it a lot less stochastic. So it is possible to view hydrates nucleation as degrees of stochastic behavior, but nonetheless stochastic.

Hydrate nucleation is the process during which small clusters of water and gas or, hydrate nuclei, grow and disperse in an attempt to achieve critical size for continued growth.

Nucleation is a microscopic phenomenon containing between tens to thousands of molecules, making it very difficult to detect experimentally. Hypothesis for nucleation is based on the principals of water freezing, dissolution of hydrocarbons in water and computer simulations based on both.

The region where the molecules nucleate and dissociate without creating critical mass for growth is called the metastable region. In other words, from the equilibrium point to the catastrophic growth point or dissolution point. (Sloan and Koh 2008)

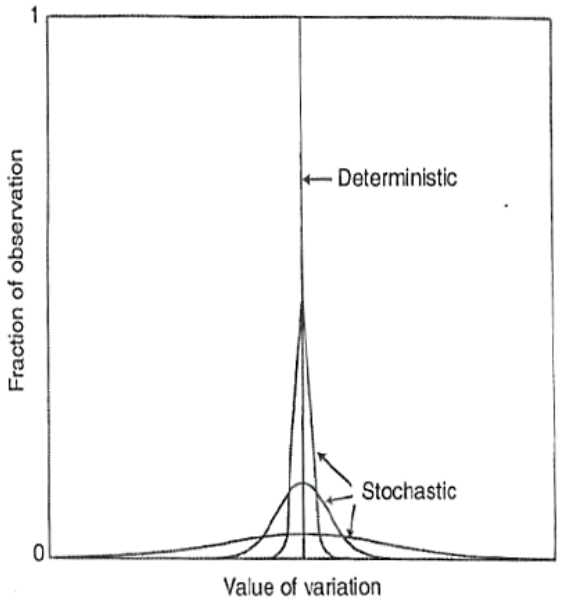

Figure 4 Deterministic vs Stochastic(Sloan and Koh 2008)

2.2.1 Homogenous Nucleation (HON)

Homogenous nucleation (HON) is a rare event in the real world and can occur with only two phases present – the solute and the forming crystal nuclei. This is a solidification of pure components, absent all impurities or foreign particles. Droplets of ultrapure water dispersing within an oil emulsion or very small droplets forming through a supersonic nozzle can accomplish this(Wyslouzil, Cheung et al. 1997). The process involves many more particles than could collide simultaneously. It is beneficial to think of this process as a series of clusters that grow until the critical size where spontaneous growth occurs. Even though HON is a rare

occurrence, much of the classical nucleation theory (Volmer and Weber, 1926) serves as a basis for most modern treatments of nucleation

As a visualization, it is possible to think of an original cluster containing two molecules that grows sequentially, one molecule at a time, until a critical size is obtained. This size has to be energetically viable to sustain growth. After this size is reached, growth occurs spontaneously. The excess Gibbs free energy (ΔG), between a small solid particle of solute and the solute in solution, may interpret this reaction.

$$\Delta G = \Delta G_s + G_v = 4\pi r^2\sigma + \frac{4}{3}\pi r^3 \Delta g_v \tag{2.1}$$

Where ΔG is the excess free energy, ΔG_s the surface excess free energy with respect to solute molecules becoming part of the crystal nuclei, and G_v is the volume excess free energy for solute molecules ending up in the bulk of the crystal nuclei. Furthermore, σ is the surface tension of the crystal-liquid interface, Δg_v is the free energy change per unit volume, and r is the radius of the solid particle.

As the hydrate grows the Gibbs free energy increases up until to the point where spontaneous growth occurs. At this point, the Gibbs free energy is denoted G_{crit}. This value is found by differentiating equation (2.1) and setting the result to zero. The following is found:

$$G_{crit} = \frac{4\pi\sigma {r_c}^2}{3} \tag{2.2}$$

Where the critical radius, r_c, is a function of the surface tension and the free energy change per volume as such:

$$r_c = \frac{-2\sigma}{\Delta g_v} \tag{2.3}$$

When considering a system where the temperature is kept constant, one may derive the following formula with respect to Gibbs free energy(Smith, Abbott et al. 2005):

$$\Delta G = \Delta H - T\Delta S \tag{2.4}$$

Initially during the nucleation phase, the entropy, here denoted by S, has a negative value. This is because energy is required to arrange the water molecules in lattices around the already created clusters. If the nuclei is to be energetically favorable to grow, the lattice structures have to be created. In other words, the system is in disarray at the start. The equivalent to the entropy, denoted S, in equation (2.4) is the surface excess free energy found in equation (2.1), denoted G_s, which in turn is a function of the cluster radius and the surface tension at the interface between solid and liquid.

The enthalpy of the system denoted, H, starts with a very low contribution in the beginning of the nucleation phase, as it is an exothermic reaction and releases energy as the reaction develops. It can also be related to the bulk volume of the cluster. As the process progresses the contribution from the bulk increases as the clusters grow. The contribution for the enthalpy is the equivalent of G_v, in equation (2.1). Being a function of the free energy change per unit volume (g_v), and volume assuming a spherical shape ($V=4/3\pi r^3$.)

Figure 5 illustrates this equation very well. Here we see an increasing ΔG in the beginning, because of the larger contribution from the surface excess free energy. As the ΔG hits the apex of the curve, one can find G_{crit} and furthermore, solve for r_c, to find the radius of which spontaneous growth occurs. As the cluster grows, the contribution from the bulk volume increases in a higher pace than that of the surface energy, and ΔG has a downward trend.

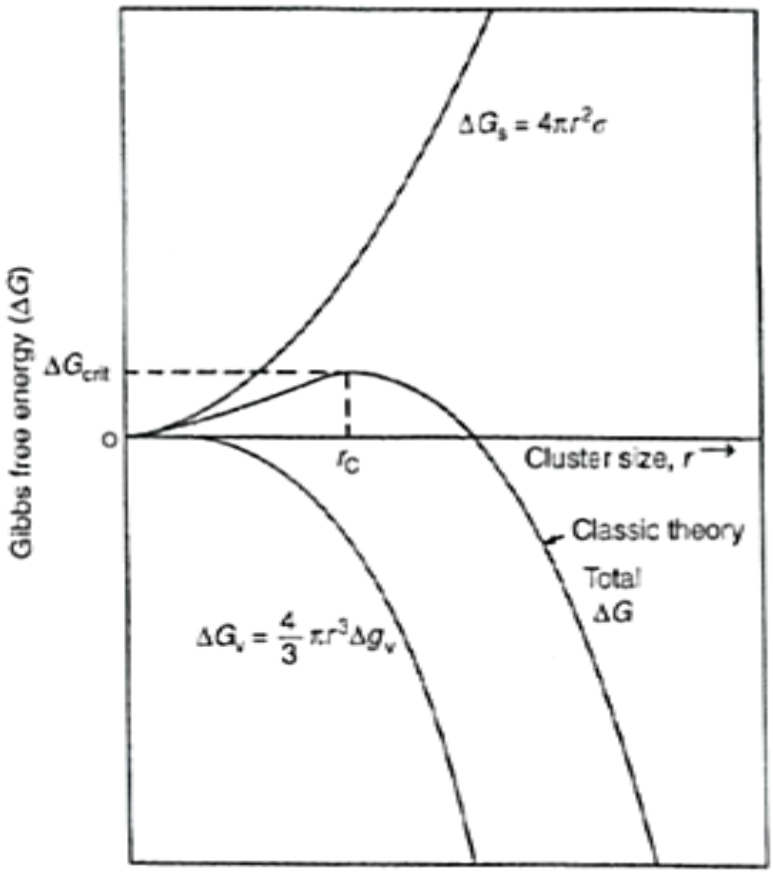

Figure 5 Relationship between bulk,-and surface excess free energy(Sloan and Koh 2008)

The growth occurring before critical size, in this bulk metastable liquid may either grow or shrink because of density and compositional changes.(Sloan and Koh 2008)

Englezos with companions (1987) modified the relationship, to find the critical radius seen in equation (2.3), using Gibbs free energy per unit volume formed:

$$(-g_v) = \frac{RT}{v_h}\left[\sum_1^2 \theta_j \, ln\left(\frac{f_{b,j}}{f_{\infty,j}}\right) + \frac{n_w v_w (P-P_\infty)}{RT}\right] \tag{2.5}$$

Where σ is the surface tension between water and ice, v_h and v_w are the molar volumes of hydrate and water respectively, θ_j the fractional filling of hydrate cages by free water, $f_{b,j}$ and

$f_{\infty,j}$ are the bulk phase experimental and equilibrium fugacities respectively, of component j at temperature T. ($P-P_{\infty}$) represents the overpressure, and n_w is the number of water molecules per gas molecule.

Using this equation, Englezos approximated a critical radius in the region of 30-170 Å, for methane hydrates.

Larson and Garside (1986) found this size to be 32 Å by using classical nucleation theory, which is in fair agreement with the approximation by Englezos.

Nerheim et al completed a set of laser scattering experiments on methane hydrates, and arrived at the approximate value of 100 Å for the critical radius.(Nerheim, Svartaas et al. 1994)

Computer simulations regarding the critical radius undertaken by Baez and Clancy (1994), and Westacott and Rodger (1998) to name a few, arrived at 14.5 Å, which is a somewhat lower value. (Sloan and Koh 2008)

2.2.2 Heterogeneous Nucleation (HEN)

Unlike HON, heterogeneous nucleation takes place with the presence of a foreign body, in the form of a dust particle, or a third surface such as a pipe wall or a gas-water interface for example. The reaction takes place at smaller supercoolings than that required of HON, and it is reasonable to assume that most of hydrate nucleations are classified as heterogeneous.

From a free energy point of view, it is more probable that the nuclei will grow on a two-dimensional surface(pipe wall, foreign particle), than in a three-dimensional area such as a free volume of water. The angle of contact, θ, between the nuclei and the surface is related to φ, which is a fraction that is multiplied to ΔG_{crit} in homogeneous nucleation to obtain a G_{crit} for HEN. This is denoted, $\Delta G'_{crit}$. The relationship follows as such:

$$\Delta G'_{crit} = \Phi \Delta G_{crit} \tag{2.6}$$

$$\Phi = \frac{[(2 + cos\theta)(1 - cos\theta)^2]}{4} \tag{2.7}$$

As mentioned before, however unlikely of naturally occurring HON, the classical nucleation theory developed serves as a very useful technique, even when regarding HEN.

When the contact angle is 180° the surface/substrate is completely nonwetting, and nothing is absorbed and $\Delta G'_{crit} = \Delta G_{crit}$. However, when the surface is completely wetting, the contact angle is 0, and $\Delta G'_{crit}=0$.

As one can deduce from equations (2.6) and (2.7), the value for $\Delta G'_{crit}$ is lowered compared to ΔG_{crit}, dependent of the fraction size. This in turn lowers the critical radius size needed for catastrophic growth, which explains why HEN occurs much more frequently.

(Kashchiev and Firoozabadi 2002) analyzed the kinetics of nucleation with one-component gas hydrates in an aqueous solution, where they maintained focus on three areas of nucleation.

1. Heterogeneous nucleation at solution-gas interface
2. Heterogeneous nucleation at solid surface
3. Homogeneous nucleation in a free volume of water

This work provided a detailed picture of the mechanisms and kinetic expressions based on classical nucleation theory. The expressions were derived for the stationary rate of hydrate nucleation, J. The work needed to form a cluster of a certain number(n) building blocks is as follows(Kashchiev and Firoozabadi 2002, Sloan and Koh 2008):

$$W(n) = -n\Delta\mu + Cv_h^{2/3}\sigma_{ef}n^{2/3} \tag{2.8}$$

Where Δμ is the supersaturation, which represents the work gained on assembling n hydrate building units into an n-sized hydrate cluster. Nucleation will only occur if $\Delta\mu > 0$. C is the shape factor, e.g. for a spherical shape like the HON, the shape factor is $(36\pi)^{1/3}$. Looking at Figure 6 regarding structures for HON and HEN, it shows that when in contact with a solid surface, the hydrate takes a semi-circular/cap form. Furthermore, when nucleation occurs at the gas-solution interface, a lens-shaped form takes place. $V_h(m^3)$ is the volume of the hydrate-building unit which consist of one gas molecule and n_w(hydration number) water molecules, σ_{ef} is the effective specific surface energy (J/m^2).

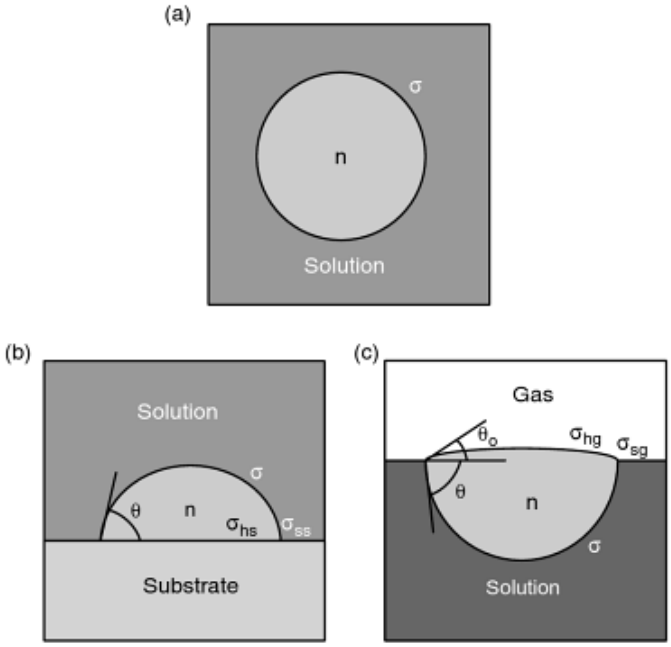

Figure 6 Illustration of : a) Spherical cluster in HON, b) cap-shaped cluster in HEN, c) lens-shaped cluster in HEN, (Sloan and Koh 2008)

2.3 Hydrate nucleation at a molecular level

In this chapter, three hypotheses regarding nucleation at the vapor-liquid interface will be discussed briefly. As the vapor-liquid interface is the most common nucleation site, most of the models have been built around that idea. These models are:

1. The labile cluster nucleation hypothesis
2. The local structuring nucleation hypothesis
3. Nucleation at interface hypothesis

2.3.1 The labile cluster nucleation hypothesis

The basis of the labile cluster hypothesis was based on the fact that water in the hydrate forming region, clusters around gas molecules as soon as it dissolves, and continue to grow to achieve critical size.

A good description of the labile cluster hypothesis is as follows; a labile cluster is an entity that readily undergoes change and the nucleation occurs as a result of agglomeration of the clusters (Sloan and Koh 2008). The labile clusters are composed of a guest molecule surrounded by 20 and 24 (sI cavity) or 20 and 28 (sII cavity) water molecules in the first solvation shell. The nucleation occurs on either the liquid or the vapor side of the interface.

2.3.2 The local structuring nucleation hypothesis

In this hypothesis, guest molecules are arranged in a configuration resembling that of the clathrate hydrate phase, due to thermal fluctuations. The structure of water molecules around locally ordered guest molecules are highly unsettled compared to that in the bulk. This thermodynamic unsettling of the liquid phase is caused by the finite temperature of the system, where the process itself is considered stochastic. The number of guest molecules in a locally ordered arrangement exceeds that of the critical nucleus. Guest-guest and host-host cluster order parameters take on values that are very close to that of the clathrate hydrate phase. This results in the formation of a critical nucleus. (Sloan and Koh 2008).

Radhakrishnan and Trout (2002) performed Landau free energy calculations to investigate the nucleation mechanisms of carbon dioxide hydrate at the water-liquid carbon dioxide interface. These calculations showed that it was thermodynamically more favorable for labile clusters to disintegrate than agglomerate, practically dismissing the labile cluster theory. This caused the need for a new hypothesis, creating the local structuring nucleation hypothesis(Radhakrishnan and Trout 2002).

2.3.3 Nucleation at the interface hypothesis

This hypothesis is more of a modification of the labile cluster hypothesis, than a stand-alone hypothesis. Long (1994) and Kvamme (1996) suggested that nucleation occurs on the vapor side of the interface. They both list a set of steps during this process. The first step is the gas molecules are transported to the interface. Here, they adsorb to the surface, before the gas molecules travel via surface diffusion to a suitable spot. This may occur at a partially completed cavity. At this stage, the water molecules form complete cages around the gas/guest molecule, before other labile clusters join in and continue growth. This happens by addition of water and gas molecules to existing cavities, or bridging of cavities along the interface, or both. This process continues until critical radius is obtained, keeping in mind that the process is not a natural progression of increasing size. As some clusters will grow and other clusters will shrink, leaving it quite arbitrary at what point this takes place.(Sloan and Koh 2008).

2.4 Enthalpy

Enthalpy is defined as a thermodynamic potential denoted H, consisting of an internal energy (U) plus volume and pressure. Any given system has a constant or given enthalpy. However, when subjected to changing scenarios, such as temperature change, that affects the internal energy or during a chemical reaction, the enthalpy value may differ from the equilibrium/initial value. Interpreting this change can describe what type of reaction is undertaken. The change in enthalpy is given by:

$$\Delta H = H_f - H_i \tag{2.9}$$

Where ΔH gives the change in enthalpy, H_f is the final enthalpy (product), and H_i is the intial enthalpy (reactants.)

If the difference is negative, that is to say $\Delta H < 0$, it is an exothermic reaction, and the system emits heat. If $\Delta H > 0$, it is and endothermic reaction, and heat is required for the reaction.

If the process is of an adiabatic nature, that is to say, without any heat or matter loss to the environment, the energy will be stored in the volume. The enthalpy can then be calculated by temperature changes in the product, and the heat capacity of the given system. Heat capacity is given by:

$$C = \frac{Q}{\Delta T} \tag{2.10}$$

Where Q is the heat, and ΔT is the temperature differential. For the case of constant pressure, one may deduce:

$$C_p = \left(\frac{\partial Q}{\partial T}\right)_p = \left(\frac{\partial H}{\partial T}\right)_p \tag{2.11}$$

If the process loses heat to its surroundings, the heat loss rate has to be known in order to calculate the enthalpy.

Different studies regarding formation enthalpy for simple and various mixtures of gas hydrates have been undertaken. Where temperature is increased and the enthalpy calculated as a function of this. In 2013, Lirio and Pessoa completed experiments with simple and mixed carbon dioxide gas hydrates. The results are shown in Table 1(Lirio and Pessoa 2013):

Table 1 Enthalpy of dissociation of simple and mixed carbon dioxide clathrate hydrates. (Lirio and Pessoa,2013)

T(°K)	P (MPa)	ΔH (kJ/mol)	n
275,3	1,59	70,8	7,9
277,2	2,01	68,2	7,4
279,2	2,55	65,2	6,9
279,9	2,86	63,1	6,6

From Table 1, a clear trend is appearing. From the start point of 275, 3 °K to the final point of 279, 9 °K, roughly a 5 °K increase, the enthalpy shows a clear decrease. So according to this work, one may deduce that the enthalpy decreases as a function of temperature.

This work is in fair agreement with Lievois doctoral thesis from 1987. Here, similar experiments with methane clathate hydates (CH_4) were completed. The distinction between the two is the different type of guest molecule, but the trend clearly appearing are of similar nature. Results from Lievois are in Table 2 (Lievois 1987):

Table 2 Enthalpy change as a function of temperature (Lievois, 1987)

T (°K)	ΔH (kJ/mol)
278,2	57,739
278,2	57,400
278,2	57,697
283,2	52,798
283,2	53,610

As seen with Lirio et al. the same trend appears in Lievois work. With a five-degree increase in temperature, the enthalpy clearly decreases. Supporting the claims that enthalpy is function of increasing temperature.

Unlike the previously mentioned results in this chapter, Anderson (2004) tested methane hydrates over an extensive range of temperatures, and arrived at a somewhat different conclusion. The results from his trials can be seen in table Table 3(Anderson 2004):

Table 3 Enthalpy of dissociation and hydration number of methane hydrate from the Clapeyron equation, (Anderson, 2004)

T/K	p/MPa	dp/dT (MPa · K^{-1})	x_{CH_4}	ΔV (m^3 · mol^{-1})	$\Delta H_{1a}(T,p)$ kJ · mol^{-1}	$\Delta H_{1b}(T,p)$ kJ · mol^{-1}	$\Delta H_1(T,p)$ kJ · mol^{-1}	ΔH_1^* kJ · mol^{-1}	n
274	2.85	0.270 ± 0.007	0.00115	7.16E – 04	52.9 ± 1.3	0.132	53.0 ± 1.3	52.9 ± 1.3	5.89 ± 0.22
278	4.28	0.414 ± 0.011	0.00146	4.60E – 04	52.9 ± 1.4	0.158	53.1 ± 1.4	52.3 ± 1.4	5.79 ± 0.23
282	6.36	0.660 ± 0.0020	0.00181	2.91E – 04	54.2 ± 1.5	0.185	54.4 ± 1.5	53.1 ± 1.5	5.93 ± 0.26
286	9.88	1.150 ± 0.037	0.00229	1.69E – 04	55.5 ± 1.7	0.217	55.7 ± 1.7	54.3 ± 1.7	6.12 ± 0.28
290	16.06	2.016 ± 0.069	0.00286	9.15E – 05	53.5 ± 1.7	0.259	53.7 ± 1.7	52.5 ± 1.7	5.83 ± 0.29
294	26.69	3.39 ± 0.12	0.00349	5.27E – 05	52.5 ± 1.8	0.287	52.8 ± 1.8	51.8 ± 1.8	5.71 ± 0.30
298	43.92	5.31 ± 0.21	0.00419	3.39E – 05	53.7 ± 1.9	0.294	54.0 ± 1.9	52.9 ± 1.9	5.90 ± 0.32
302	69.68	7.62 ± 0.31	0.00499	2.36E – 05	54.2 ± 2.0	0.294	54.5 ± 2.0	53.7 ± 2.0	6.02 ± 0.34
306	105.18	10.17 ± 0.44	0.00583	1.75E – 05	54.5 ± 2.2	0.266	54.8 ± 2.2	53.2 ± 2.2	5.94 ± 0.36
310	151.70	13.28 ± 0.60	0.00661	1.32E – 05	54.4 ± 2.3	0.200	54.6 ± 2.3	52.6 ± 2.3	5.85 ± 0.38
314	214.40	18.74 ± 0.89	0.00723	9.29E – 06	54.7 ± 2.4	0.081	54.7 ± 2.4	52.5 ± 2.4	5.83 ± 0.40
318	311.12	31.6 ± 1.6	0.00744	5.45E – 06	54.7 ± 2.6	–0.114	54.6 ± 2.6	52.5 ± 2.6	5.82 ± 0.44

Here we see the results from a very wide temperature range, all the way from 274 to 318 °K. During this 44-degree increase in temperature, the enthalpy remains more or less constant with very little variation. Which is in fair agreement with the work done by Gupta et al, who initiated experiments with methane hydrates. The results are shown in Table 4(Gupta, Lachance et al. 2008):

Table 4 Measurements of methane hydrate heat of dissociation using high pressure differential scanning calorimetry, (Gupta et al. 2008)

	P (MPa)	T_{onset} (K)	X_I	X_H	ΔH_d (J/gm hydrate)	ΔH_d (J/gm water)	ΔH_d (kJ/mole gas)
Test 1	5.5	280.60	0.01	0.99	442.21	508.29	54.90
Test 2	9.8	285.65	0.15	0.85	420.60	483.45	55.21
Test 3	12.8	288.15	0.04	0.96	433.96	498.80	53.87
Test 4	13.2	288.45	0.01	0.99	428.58	492.62	53.20
Test 5	15.0	289.85	0.24	0.76	455.01	523.00	56.48
Test 6	18.5	292.16	0.22	0.78	441.39	507.35	54.79
Test 7	19.3	291.65	0.05	0.95	448.02	514.97	55.62
Average					438.54	504.07	54.44
Std deviation					11.73	13.48	1.46

X_I and X_H shows the ice and hydrate phase fractions.

Comparing all of these results, they (Anderson, Gupta et al., Lievois) show agreement of the values of enthalpy at specific temperature points, but are somewhat differing when addressing enthalpies dependence of temperature. Lirio experimented with carbon dioxide (CO_2), getting slightly elevated enthalpy values. Anderson and Gupta et al. both show a sort of consistency for their enthalpy values, whilst Lirio et al. and Lievois both show a declining enthalpy trend as a function of increasing temperature.

2.5 Crystal growth process

After the initial nucleation, comes the hydrate growth process. Unlike the nucleation phase, which is stochastic and very difficult to predict, the growth phase is more predictable. The hydrate crystal growth process may be sub-categorized into four points. These are:

1. Single crystal growth
2. Hydrate film/shell growth at the water-hydrocarbon interface
3. Crystal growth with interfacial agitation
4. Growth of metastable phases

In the upcoming chapters, point one and two will be described in depth, whilst points three and four will be neglected.

2.5.1 Single crystal growth

This particular situation is hydrates, which grow as single crystals during low driving forces in water-hydrocarbon solutions. This type of growth is useful when investigating the effects of additives on hydrate crystal growth and morphology. Some types of hydrates are easily manufactured in the laboratory by this process, e.g. single crystals of tetrahydrofuran (THF) or single crystals ethylene oxide. They are both completely miscible in a water solution, and can be isolated for structural analysis. In contrast however, are the gas hydrates, which are difficult to isolate. Only a few successful single crystals from natural gas have been obtained. (Sloan and Koh 2008)

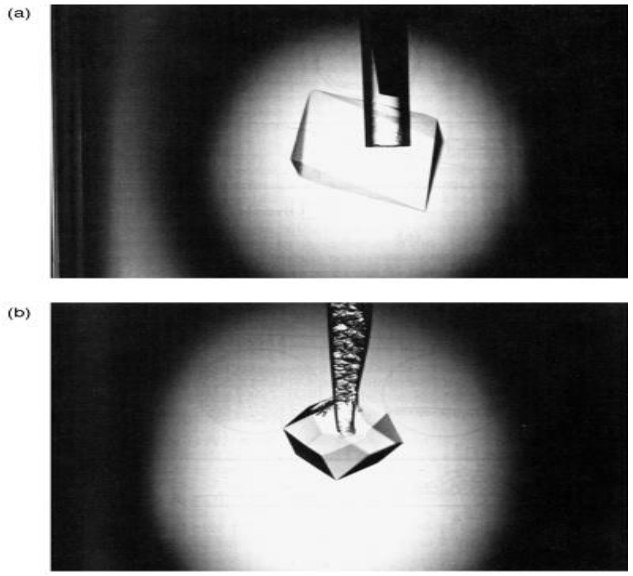

Figure 7 Single crystals for structure I and structure II, (Sloan and Koh, 2008)

Looking at Figure 7, one can see two specimens of isolated crystals representing both sI and sII. Picture (a) shows a single crystal hydrate grown from a stoichiometric solution of THF representing sII. Picture (b) shows a single crystal hydrate grown from a stoichiometric solution of ethylene oxide, representing sI. They are both at rested conditions. The single crystals display (110) and (111) planes for structures I, and II, respectively. The crystals exhibited on this figure are a result of the slowest growing planes, as it is important to know that the rapidly growing planes quickly disappear, whilst the slow growing become the observable. Smelik and King (1997) reported similar results, with respect to single crystal growth, in their high pressure single crystal system.

It was hypothesized by Smelik and King that the planes (111) in sII, and (110) in sI are the slowest growing planes due to their predominant hexagonal faces relative to other crystal planes. This is emphasized because hexagonal faces are considerably more strained, 120° O-O-O angles, than e.g. pentagonal faces (108°), tetrahedral faces (109°), or the water angle (H-O-H with 104,5°).

2.5.2 Hydrate film/shell growth at the water-hydrocarbon interface

Hydrate growth usually initiates at the water-hydrocarbon interface, and measurement of the film/shell created at this interface can provide good predictive growth mechanisms, which in turn can be incorporated into realistic models. Extensive research is performed on this particular subject. As seen in Table 5:

Table 5 Collection of interfacial growth systems

Hydrate film/shell measurement	**Water-hydrocarbon interfacial system**	**Researcher(s)**
Film growth at liquid water-hydrate former interface	Water-Methane	(Smelik and King, 1997), (Makogon et al., 1998), (Freer, Sami Selim et al. 2001), (Taylor 2006)
Film growth at liquid water-hydrate former interface	Water-fluorocarbon	(Sugaya and Mori 1996), (Ohmura, Kashiwazaki et al. 2000), (Ito, Kamakura et al. 2003)
Film growth at liquid water-hydrate former interface	Water-carbon dioxide	(Uchida, Ebinuma et al. 1999), (Hirai et al. 2000), (Mori 2001), (Uchida, Ikeda et al. 2002), (Hirai and Sanda 2004)
Shell growth on gas(hydrate former) bubble surface	Natural gas bubble in salt water	(Maini and Bishnoi 1981), (Topham 1984)
Shell growth on gas(hydrate former) bubble surface	Air bubble-ice interface	(Salamatin, Hondoh et al. 1998)
Shell growth on gas(hydrate former) bubble surface	Hydrofluorocarbon gas bubble in water	(Nojima and Mori 1994)
Shell growth on liquid hydrate former droplet surface	Hydrofluorocarbon droplet in water	(Kato et al. 2000), (Ohmura, Shigetomi et al. 1999), (Ohmura, Ogawa et al. 2003)

Shell growth on liquid hydrate former droplet surface	Cyclopentane droplet in water	(Taylor 2006), (Taylor, Miller et al. 2007)
Shell growth on liquid hydrate former droplet surface	Liquid carbon dioxide droplet in water	(Shindo, Lund et al. 1993)
Shell growth on droplet surface of aqueous solution of hydrate former	Aqueous THF solution droplet in n-decane	(Taylor 2006)
Shell growth on water droplet surface	Water droplet in methane or carbon dioxide gas	(Servio and Englezos 2003), (Moudrakovski, McLaurin et al. 2004)
Shell growth on water droplet surface	Water droplet in fluorocarbon gas	(Fukumoto, Tobe et al. 2001)

If more in depth information is required about a particular experiment, the reader is referred to the reference list, or (Sloan and Koh 2008) where the particulars can be attained.

Common features among this vast list, is the morphology changes are generally similar regardless of the hydrate former. However, the driving forces can affect the morphology and there are similar features between growth behavior at a water-hydrate former planar interface and at the surface of a liquid droplet.

In 2003, Servio and Englezos examined methane and carbon dioxide grown on water droplets. Specifically, pressure as a driving force on the morphology. They completed experiments with both high,-and low driving forces. During the high driving force, the pressure was 2150 kPa, and within 5 seconds after nucleation, the droplet appeared. The appearance was roughened with many fine needle-like crystals, pointing away from the interface. To prevent the droplets from wetting the surface, a Teflon-coated 316 stainless steel surface was placed.

During low driving forces (1000 kPa), the result was in contrast. The droplets appeared smooth and shiny, with none of the needle-like crystals. The conclusion of this result was that during high driving forces, growth occurred rapidly and at many different places, making it quite unpredictable. On the other hand, at low driving forces the growth was lengthy and more predictable. This was in fair agreement with Mullins (2001) suggestion that the number of

nuclei being formed per unit time per unit volume increases as a function of supersaturation. Which in turn, is equivalent to the driving force.

Servio and Englezos list three main points deducted from this experiment with respect to high driving forces:

1. The appearance of a hydrate shell around the water droplet with needle-like crystals, which continue to grow in both width and thickness ten hours after nucleation.
2. The crystal needles eventually collapse onto the hydrate layering covering the droplet
3. An appearance of depression in the hydrate layer surrounding the water droplet, which could happen between 10 hours after nucleation to a couple of days.

Figure 8 illustrates the differences in growth when subjected to different driving forces, where the left picture shows the needle-like shape appearing during high driving forces, and the right shows the smooth shape undertaken when subjected to low driving forces.

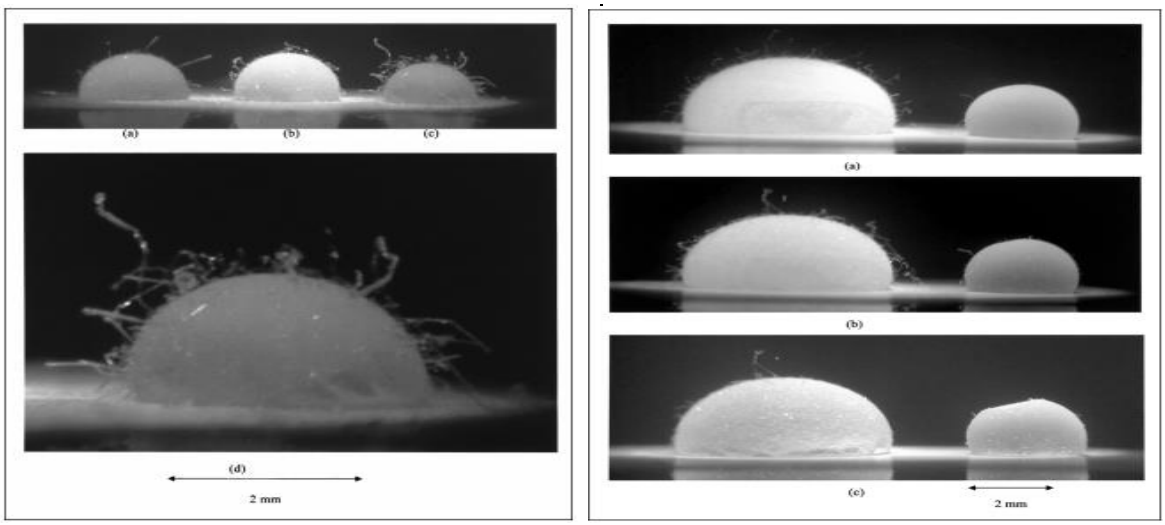

Figure 8 Difference between growth when subjected to different driving forces, (Servio and Englezos 2003)

2.6 Correlation between stirring rate and the inner heat coefficient

In 2009, Ebrahimi et al. conducted experiments which focused on heat transfer and what impact different stirring rates contributed to this. The experiments were conducted in cylindrical titanium test cells, with a three-headed rotating blade at the center, which supplied the rotational effect. Using constants, where the only variable was the stirring rate, the following correlation was established (Ebrahimi, Bandari et al. 2009):

$$\frac{h_i D_T}{K} = 0{,}37 * (Re)^{0{,}67} * (\mathrm{Pr})^{0{,}33} \tag{2.12}$$

When solved for the inner heat coefficient, hi:

$$h_i = 0{,}37 * (Re)^{0{,}67} * (\mathrm{Pr})^{0{,}33} * \frac{K}{D_T} \tag{2.13}$$

Where :

D_T = Diameter of the titanium testing cell, m

K = Thermal conductivity, W/m*K

Pr = Prandtl's number. The dimensionless ratio of momentum diffusivity to thermal diffusivity, given by:

$$Pr = \frac{\mu * C_p}{K} \tag{2.14}$$

where μ is the viscosity in Pa·s, C_p is the specific heat capacity in J/kg·K, and K is the thermal conductivity.

Re = Reynolds number. Dimensionless number to predict flow regime, given by:

$$\mathrm{Re} = \frac{\rho N {D_a}^2}{\mu} \tag{2.15}$$

where ρ is the fluid density in kg/m^3, N is the rotation given in 1/s, D_a is the rotating blade diameter in m, and μ is the viscosity in Pa·s.

2.7 Conduction and convective heat transfer

In this chapter, the phenomenon's conduction and convective heat transfer will be presented briefly.

Conduction may be viewed as the transfer of energy from highly energetic particles to less energetic particles of a substance due to interactions between particles. When a substance is heated, e.g. gas, the particles will gain more energy, which will increase the particles motion in the form of translation, rotation and vibration. In the presence of another substance, e.g. a titanium test cell, the highly energetic particles will collide with the less energetic particles, transferring energy in the process. With a temperature gradient, this energy is in the form of heat. This process will continue transferring energy from high to low, until an equilibrium is reached. The energy transfer is called diffusion, or random molecular motion.

Convective heat transfer follow the same principles as conduction, i.e. diffusion, but also take into account the energy transferred from the bulk, or macroscopic motion of the fluid. Convection occurs when warm areas of a liquid or gas rise due to density changes into cooler areas, and the cooler areas take the initial spot of the risen warm areas. This is a continuous process. (Incropera and DeWitt 1996)

3 Hydrate growth and heat transfer modelling

Factors contributing in the growth of a gas hydrate can be generalized into three categories:

1. Intrinsic growth kinetics
2. Mass transfer limited kinetics
3. Heat transfer limited kinetics

In the following chapter, many different models will be discussed, but as (Sloan and Koh 2008) lists, it is important to remember three points when reviewing any model:

1. Hydrate nucleation is a stochastic and unpredictable process. The data is significantly scattered, especially at conditions with low driving force under isothermal conditions.
2. Every model created may be apparatus dependent so also the growth process, and there are no assurances that the model will relate to real life situations, such as in an oil and gas pipeline.
3. Most data attained, have been collected for structure I hydrates, but in gas pipelines the most frequent gas hydrate takes on structure II. The crystal structure and the gas composition has a large impact on the rate of growth.

At the present date, the role of kinetics tied to heat,-and mass transfer is thought to be the main limiting factors in hydrate growth. Whereas the role of intrinsic growth kinetics is such a rapid one, that it does not limit growth (personal communication with T.M Svartås, 2014). Table 6 displays some of the work completed with respect to growth models:

Table 6: Summary of growth models

Growth Models	**Driving force/model features**	**Researchers**
Growth kinetics	$(f-f_{eq})$	(Englezos, Kalogerakis et al. 1987, Englezos, Kalogerakis et al. 1987)
Growth kinetics	$(f-f_{eq})$ with minor modifications to Englezos' model	(Malegaonkar, Dholabhai et al. 1997)
Mass transfer	$\left(x_{int}^{i} - x_{b}^{i}\right)$ with simplification to Englezos' model	(Skovborg and Rasmussen 1994)
Mass transfer	Based on phase field theory	(Svandal, Kvamme et al. 2005)
Mass transfer	Based on Monte Carlo cellular automata	(Buanes, Kvamme et al. 2006)
Heat transfer	Curved film front growth on water-hydrate former interface	(Uchida, Ebinuma et al. 1999)
Heat transfer	Curved film front growth on water-hydrate former fluid interface	(Mori 2001)
Heat transfer	Straight film front growth on water side of water-hydrate former interface	(Freer, Sami Selim et al. 2001, Mochizuki and Mori 2005, Mochizuki and Mori 2006)

3.1 The Englezos-Bishnoi model

The Englezos-Bishnoi model is based on growth kinetics as Table 6 tells us. However, in more recent times, the role of intrinsic kinetic growth in hydrates is suggested to play a minor role compared to heat,-and mass transfer in real life turbulent environments, e.g. oil/gas pipelines. Nonetheless, it is included as it has served as a basis for several models developed at later stages.

Englezos et al. generated a kinetic model for methane, ethane and their mixture to correlate with hydrate growth data in a high pressure-stirring reactor. Englezos assumed three steps in hydrate formation:

1. The transport of gas goes from the vapor phase to the bulk of the liquid
2. The diffusion of gas goes from the bulk of the liquid, through the boundary layer around hydrate particles.
3. Finally, an adsorption reaction whereby gas molecules are incorporated into the already created crystal lattices/water framworks.

The model by Englezos et al. is described as such:

$$(dn_i/dt)_p = K^* A_p (f^b - f^{eq}) \tag{3.1}$$

With:

$$\frac{1}{K^*} = \frac{1}{k_r} + \frac{1}{k_d} \tag{3.2}$$

Where:

$(dn_i/dt)_p$= Number of gas molecules consumed per second by the hydrate

A_p= Surface area of each particle

f_i= Fugacity of component i in the bulk liquid

f_i^{eq}= Equilibrium fugacity of component i in the liquid at the hydrate interface

K^*= Hydrate formation growth rate constant, describing a combined rate for diffusion and adsorption

k_r= reaction rate constant

k_d= mass transfer coefficient through the film around the particle

$(f^b - f^{eq})$ = The overall driving force

This model was adopted by Malegaonkar (1997) and by Skovborg and Rasmussen (1994), where they both integrated some modifications. The distinction between Malegaonkar and Englezos' model was the correction of carbon dioxides high solubility in water (Malegaonkar, Dholabhai et al. 1997)

Whenever using a model, it is vital to know the restrictions that follow, as no clear universal model exists. The case of the Englezos-Bishnoi-Malegaonkar the following restrictions exist:

1. The entire model was tailored around the parameter K^*, which is for the simple hydrate formers such as methane, ethane, carbon dioxide. All of these components form sI hydrates, encouraging caution when using the model with sII and sH.
2. When calculating the critical radius, the hydrate was assumed to stay at the equilibrium pressure instead of the system pressure, ignoring the final term in ΔG.
3. As current knowledge suggests, intrinsic kinetics plays a minor role in hydrate formation in real-life systems. (Sloan and Koh 2008)

In addition to these restrictions, Skovborg and Rasmussen list some additional points, which is shown in chapter 3.2.

3.2 The Skovborg-Rasmussen model

Contrary to the Englezos-Bishnoi-Malegaonkar model, Skovborg and Rasmussen created a model based on mass transfer. They place the original Englezos-Bishnoi as a basis, but with modifications. The disagreement is with the Englezos-Bishnoi model is summarized below:

1. Englezos-Bishnoi secondary nucleation constant was very low (10^{-3}), implying that no second nucleation took place, and that all particles were the same size and had the same growth rate. The crystallization population was therefore removed from the model entirely.
2. The value of the hydrate formation growth rate constant, K^*, may have been too high. Skovborg suggested that this was caused by errors in the mass transfer coefficient through the liquid film, k_l, and furthermore that the value of k_l was wrong. A 50 % error in the value of k_l, can create an error in the value of K^* by an order of two magnitudes.
3. The model is designed for linear growth after nucleation. Where the starting time is from the visual observation of hydrates, also called the turbidity point. The critique from Skovborg was, when a model is extrapolated by an order of magnitude, one can expect increasing growth observed with time, in contrary to long-time data.
4. The model is very sensitive to the amount of moles consumed, and this exact number is very difficult to obtain at the turbidity point. (Skovborg and Rasmussen 1994)

With all these restrictions in place, Skovborg and Rasmussen implemented a new model, with mass transfer as the foundation. The assumption was that the entire hydrate process could be described by the mass transfer restriction of gas through the liquid film at the interface. This gave them the following model:

$$\frac{dn}{dt} = k_l A_{(g-1)} c_{wo} (x_{int} - x_b) \tag{3.3}$$

where:

$A_{(g-1)}$= Gas-liquid interface area (value obtained from the work of Englezos)

C_{wo}= Initial concentration of water

x_{int}= bulk liquid mole fraction of the component

3.3 Heat transfer models

The models created for the heat transfer occurring in hydrate formation is focused on the lateral growth of the hydrate film across a water-gas interface. Several different models are described, as the upcoming subchapters will show.

3.3.1 The Uchida model

The basis for this model was a water droplet submerged in liquid carbon dioxide. Hydrate crystals form at the front of the film, and the front is maintained at the three-phase equilibrium temperature. Uchida et al. list some assumptions for this model:

1. There is a steady heat transfer from the front, to the water and guest fluid
2. The heat generated by hydrate formation, which is an exothermic process, balances the heat removed from the front.

With these assumptions, Uchida et al. related the linear growth rate of the film across the interface, denoted v_f, with the hydrate thickness (δ) and the degree of subcooling (ΔT). The hydrate film thickness is estimated by fitting the v_f - ΔT plot to the corresponding experimental data. Figure 9 illustrates the model Uchida proposed (Uchida, Ebinuma et al. 1999, Sloan and Koh 2008).

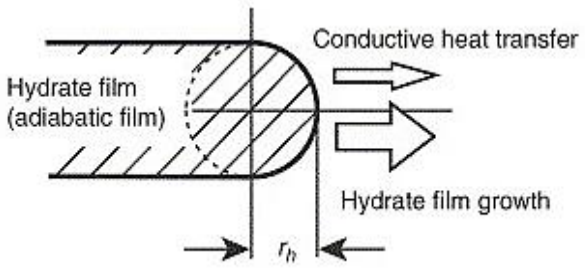

Figure 9 Hydrate film model by Uchida et al. (Mochizuki and Mori, 2006)

3.3.2 The Mori model

This model is as Uchida's model based on lateral growth of the hydrate film. This takes place in a stagnant water pool with a guest fluid. The first real difference from the Uchida model, is

the topic of heat removal, created by hydrate formation. Countercurrents, which travel at the same velocity as the film front, but in the opposite direction, remove the heat by steady convective heat transfer. An illustration of the Mori model can be seen in Figure 10.(Mori 2001, Sloan and Koh 2008)

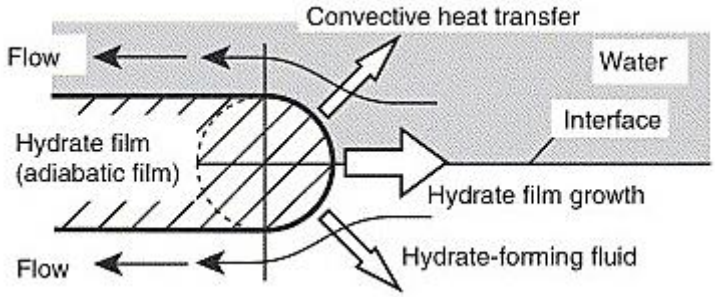

Figure 10 Hydrate film by Mori, (Mochizuki and Mori, 2006)

3.3.3 The Freer Model

This particular model was based on experimental data conducted on methane hydrates and specifically the film growth rate at the methane-water interface. The film velocity was modeled, with the assumption of one-dimensional conductive heat transfer from the front of the hydrate film, extending all the way to the water phase beyond the front. When calculating the film velocity, it was far lower than the experimental value. Freer therefore concluded with that the film growth was controlled by the kinetics of hydrate formation. An illustration of Freer's model is seen in Figure 11.(Freer, Sami Selim et al. 2001, Sloan and Koh 2008)

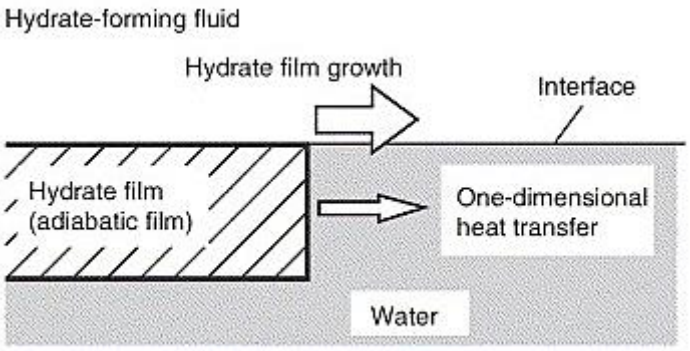

Figure 11 Hydrate film model by Freer, (Mochizuki and Mori, 2006)

3.3.4 The Mochizuki and Mori model

In their paper from 2006, Mochizuki and Mori list a number of critiques of the previous models listen in chapter 3.3, before proposing a new model.

When addressing Uchida's model, the concern was the formulation regarding the conductive heat transfer from the film front. This had, as expressed by Mochizuki and Mori, little physical reasoning. It was concluded that Uchida's model could be used to determine the hydrate film thickness (δ), more than to describe the lateral film growth.

Mori's model from 2001 was also under some critique concerning the countercurrent. Mochizuki and Mori states that since the hydrates density is very similar to that of the water, displacement is an unrealistic event. Furthermore, the water would be transformed into hydrate structure at its location. Since the thermal conductivity of the guest fluid is very small, the role in removing heat would be a minor one.

Freer's model was also received some critique, due to the shape of the film front. In contrast to the other models mentioned here, Freer chose a straight edged film front. Mochizuki and Mori suggested that due to the thin nature of the film front, the shape would most likely take on a bulging shape with strong curvature.

After reviewing all these models, Mochizuki and Mori finally proposed a new model. Similar to Freer's model, the assumption was that the hydrate film existed on the water phase of the water-guest interface. The hydrate film is homogenous on a microscopic scale, and the water and gas phase extended infinitely. Hydrate growth only occurs on the front of the film and the lateral growth exceeds the thickening/thinning of the film. The temperature at the film front stays within the three-phase equilibrium temperature. The rate of heat removal is balanced out by the heat generated by hydrate formation, and there is no liquid movement by either the water, or the guest. The model can be described by equation (3.4):

$$\rho_h \delta \Delta h_H v_f = \int_0^{\delta} \left(\lambda_h \frac{\partial T}{\partial x}\Big|_{x=x_{h-}} - \lambda w \frac{\partial T}{\partial x}\Big|_{x=x_{h+}} \right) dy \tag{3.4}$$

where:

δ = Hydrate film thickness

$\partial T/\partial x|_{x=xh-}$ = Hydrate temperature gradient (The x denotes the position of the hydrate film front)

$\partial T/\partial x|_{x=xh+}$ = Water temperature gradient

Δh_H = Heat of hydrate formation per unit mass of hydrate

λ_h, λ_w = Thermal conductivity of hydrates and water respectively

Machizuki and Mori noted that the hydrate growth is usually not of a linear nature, but of a radial kind. However, the experimental values for the hydrate film velocity, v_f, was in fair agreement, regardless of using a straight or semi-curved front. As was the heat released, even though the semi-circular film front emits less heat than the straight front. The Mochizuki-Mori model was also tested with data from previous experiments from Freer (2001), Uchida (1999), Makogon (1998) and Taylor (2006). The comparisons in film thickness were in fair agreement for all cases. An illustration of the Mochizuki-Mori model is seen in Figure 12 (Mochizuki and Mori 2006, Sloan and Koh 2008).

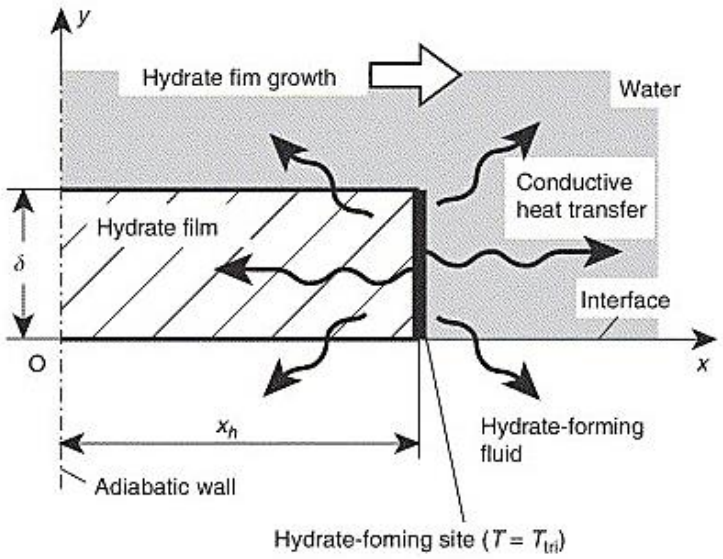

Figure 12 Hydrate film model by Mochizuki and Mori, (Mochizuki and Mori, 2006)

3.4 Shell model considering intrinsic kinetics, mass,-and heat transfer

In 2011, Shi et al. created a shell model, which tries to describe the inward and outward growth of hydrate formation around an emulsion, consisting of a certain water cut and condensate oil. In this model, the three main features, or limitations, in hydrate formation were considered. These are intrinsic kinetics, mass,-and heat transfer.

The experimental phase was done with an emulsion of varying water cuts and an oil condensate. Natural gas was injected, until the liquid was saturated. The result showed that with higher water cuts, the saturation process happened much quicker, as did the rate of gas consumption. Furthermore, it was assumed that the complete saturation happened before any visual signs of hydrate formation. The amount of gas dissolved in the hydrocarbon solution was calculated by flash equations, and were found to be decreasing with rising water cuts. With the measured gas consumption, the water conversion rates could be calculated, but the relationship was not fully clear. This could be due to that the water conversion rate depended on several other factors. Among them, the amount of dissolved gas and the surface area of the particles.

When modelling, several factors had to be taken into account. Such as thermodynamic conditions with enough driving force (growth kinetics), continuous mass transfer of gas and water, and the rapid heat transfer regarding the exothermic reaction occurring in hydrate formation.

Initially, after the water droplet is covered with a hydrate film, several processes have to take place in order for continuous growth. Specifically the diffusion of gas to the inner part of the hydrate shell, and the capillary driven flow of water to the outside of the shell. Furthermore, the conductive heat transfer of the surrounding liquid balances the heat exerted by the hydrate formation.

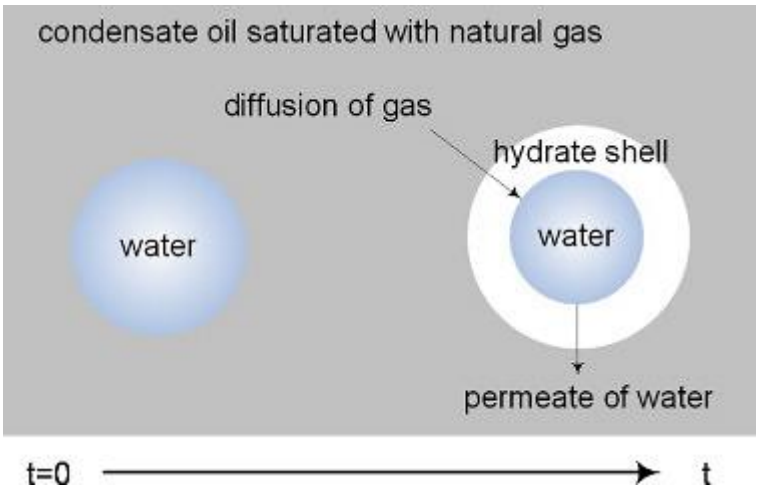

Figure 13 Illustration of the shell model, (Shi et al. 2011)

The model has a basis of two simultaneous growth processes, the inward growth, and the outward growth. For the inward growth process, the interface is imagined at the hydrate/water connection point, where the water consumption is estimated and the outer diameter of the shell is kept constant. The model then predicts for inward growth:

- Gas diffusion rate through the H/W interface, based on calculated concentrations of each gas component in the emulsion liquid, and the temperature conditions.
- The amount of gas and water consumed by the inward hydrate formation process, utilizing a simplified kinetic growth model, with a set concentration parameter for the dissolved gas and by that the water consumption rate was proportional to the droplet radius.
- Estimating the mass conservation at the H/W interface by using an intrinsic kinetic model. Assuming that that the rate of gas diffusion through the shell was instantly balanced by the hydrate formation, and that the gas consumption rate was in direct proportion to the water consumed by hydrate formation.

The next and final part of the model considers the outwards growth. It was assumed that water from the core of the water droplet permeates through the film shell and undergoes an instantaneous phase transformation into the hydrate phase. This due to the fact that the gas concentration at the oil/hydrate interface should be sufficient to accommodate formation and

growth. The rate of this phase transition is dependent of the amount of water that permeates. The following steps exist with respect to outward growth:

- Estimating the temperature profile around the water droplet, with the assumption that the heat exerted by hydrate formation is transferred to the water droplet and the surrounding oil. Creating a constant temperature profile for the hydrate film, which means that no heat is stored inside the film.
- Calculating the film thickness by using the radius found in the inward growth calculations and the outer radius measured at the last time step.

This extensive model correlated well with Shi et al.'s particular experimental data (Shi, Gong et al. 2011).

4 Simulation procedure

Professor Runar Bøe at UiS created the model of choice for this particular thesis. The general idea behind this model is to describe hydrate growth as a function of convective heat transfer and energy balance. Whereas the raw data utilized, is collected from the vast amount of experiments completed by MSc candidate Therese Nordbø in 2013.

4.1 Background of the model used

All of the experiments were carried out in cylindrical test cells, made up by titanium walls with a rotating blade inside. The cell was completely engulfed by a cooling tank, where cold water continuously flowed to maintain constant temperature. Thermometers were placed at (i)the gas entrance point (T_g), (ii)close to the interior wall inside the cell (T_w), and at (iii)the inlet and outlet of the cooling water (T_b). The geometry of the cells led to the assumption of a radial heat flow profile, where it was assumed that the heat exerted by hydrate formation was uniformly distributed along the horizontal plain. For simplicity, any heat loss through the top lid (z-direction) was neglected.

In order to estimate the energy flow through the titanium cell wall, parameters have to be set. In particular the temperature differential between the interior,-and exterior cell wall. In order to decide ΔT, the related coefficients need to be decided. They consist of:

- The heat transfer coefficient between the water and the inner wall under turbulent flowing conditions, hi.
- Conductivity through the titanium cell wall, which is a constant.
- The heat transfer coefficient for the outer wall. Estimated by the relationship between the cold flowing water and the outer wall, ho.

The other parameter needed is the energy balance relationship. The outflowing heat created by the exothermic reaction of hydrate formation should be equal to the amount of enthalpy produced by the same formation. This is approximated by:

- The enthalpy content can be calculated for each component inside the cell by using the specific heat capacity, the amount (mass), and the inside temperature.
- Any enthalpy change in the mass phase is added to the heat flow out of the cell. This sum is the same as the flow into the cell. By finding the heat flow into the cell, the released formation enthalpy from hydrate formation can be found, as their relationship must be equal.
- The amount of moles of gas consumed during this process to maintain constant pressure. The inflow of gas is controlled by a pressure switch, which opens when pressure is dropped, i.e. when gas is consumed by hydrate formation.
- Formation enthalpy is determined by number of moles consumed related to estimated energy produced in the cell.

The border condition for the outer wall is formulated by the product of heat flux and the outer heat coefficient including the sum of the differential between the outer wall temperature and the cooling bath.

For the inner wall facing the reaction, the assumption is that the heat generated by hydrate formation is partly distributed to the reaction chamber, and partly to the inside wall, resulting in temperature increase for both.

The heat of reaction, i.e. the heat generated by hydrate formation can be expressed through heat balance, which follows:

Convection at inner border:

$$\dot{q}_{conv} = h_i * A_i * (T_i - T_o) \tag{4.1}$$

Heat of reaction:

$$\dot{q}_R = \dot{q}_R \tag{4.2}$$

Sensible heat increase:

$$\dot{q}_i = (m_w C_w + m_H C_H + N_G C_{p,g}) \frac{\partial T}{\partial t}\Big|_i \tag{4.3}$$

Summing with proper signs:

$$\dot{q}_R - \dot{q}_i = \dot{q}_{conv} \tag{4.4}$$

Arranging to get heat of reaction alone, yields:

$$\dot{q}_R = \left(m_w * c_w + m_H * c_H + N_G * c_{p,g}\right) \left.\frac{\partial T}{\partial t}\right|_i + h_i * A_i * \Delta T \tag{4.5}$$

where: m_w and m_H is the mass of water and hydrate respectively, c_w and c_H is the heat capacity for water and hydrate respectively, N_g is molar amount of gas, $c_{p,g}$ is the specific heat capacity for gas, $\left.\frac{\partial T}{\partial t}\right|_i$ is the inner temperature gradient, h_i is the inner heat transfer coefficient, A_i is the inner wall surface, and the temperature differential is the result of difference between interior cell temperature and inner wall temperature.

4.2 Data analysis

When reviewing the data sets, it was especially six columns of interest for the simulating preparation, which were:

- Experimental time, i.e. the amount of running time of the experiment [min]
- The pressure [bar]
- The measure temperature of the inflowing gas [°C]
- The temperature of the water inside the cell [°C]
- The temperature of the cooling bath [°C]
- The flow rate of gas [nml/min]

The sampled data is gathered as a result of the first clear observation of hydrate formation. That is to say, when the flow rate of gas spikes from a value close to zero, up to a value in the hundreds. After this observation, data roughly from one minute before the observation, and two minutes after the observation is selected. This short time-span is selected to investigate the behavior inside the cell before too much hydrate slurry is created. The hydrate slurry changes many parameters, making it far more difficult to predict and estimate any clear

behavior. The data is then transferred over to a template with built in formulas, which predict the following:

- The total amount of gas in moles. Obtained by using the ideal gas law, where the only shifting variables is the temperature of gas and the pressure. The ideal gas law is as follows:

$$N_g = \frac{PV_g}{zRT_g} \tag{4.6}$$

where n is the amount of moles, P is the pressure at a given point, V_g is the volume of the gas, z is the compressibility factor, R is the universal gas constant, and T_g is the temperature of the gas at a given point.

- The different rates with respect to consumption and inflow, which are as follows:

    - Inflow rate of gas in mole/min. Basically converting the initial experimental reading of nml/mole per time-step [1 time-step = 0,05min/3sec]:

$$\dot{N} = \dot{V_g} * 4{,}46\dot{1}5 * 10^{-5} \tag{4.7}$$

    - The rate of change in total gas amount:

$$\dot{N_g} = \frac{dN_g}{dt} \tag{4.8}$$

    - The consumed gas rate in hydrate formation:

$$\dot{N_R} = \dot{N} - \dot{N_g} \tag{4.9}$$

- The consumed water rate in hydrate formation:

$$\dot{N}_w = n * \dot{N}_R \tag{4.10}$$

where n is the total amount of water molecules per gas molecule in a hydrate

- Hydrate growth rate:

$$\dot{N}_H = (1 + n) * \dot{N}_R \tag{4.11}$$

- The total amounts of water and hydrate, given in moles, calculated by the trapezoidal rule. In other words, finding the mean of a definite integral with set boundaries. These amounts, in addition to the percentage of water converted is given as follows:

- The molar amount of water per time-step:

$$N_w(t) = \int_0^t \dot{N}_w \, dt \tag{4.12}$$

- The molar amount of hydrate per time-step:

$$N_H(t) = \int_0^t \dot{N}_H \, dt \tag{4.13}$$

- The water percentage converted:

$$\%\, Water\ converted = \frac{Initial\ water\ [moles] - N_w(t)}{Initial\ water\ [moles]} * 100\% \tag{4.14}$$

- The amount of thermal mass for the components gas, water, and hydrate with units J/K, is given by:
  - Thermal mass for gas:

$$M_{Th,g} = N_g(t) * C_{p,g} \tag{4.15}$$

- Thermal mass for water:

$$M_{Th,w} = N_w(t) * M_w * c_w \tag{4.16}$$

- Thermal mass for hydrates:

$$M_{Th,H} = N_H(t) * M_H * C_H \tag{4.17}$$

Where $N_{g,}$ N_w, and N_H are the molar amounts of gas, water and hydrate respectively at a given time-step. $C_{p,g}$, C_w, and C_H are the specific heat capacities with same denotations with respect to component as above, and M_w and M_H are the molar masses for water and hydrate respectively.

With all these calculations in place, the template then converts the data needed for simulation into vectors, where they are ready to be transferred to the simulation program.

In this thesis, MatLab was the preferred simulation program. The vectors or input data for MatLab were calculated in the following manner:

Ti, inside temperature in °C. Calculated by using the temperature of gas and water, as well as the thermal mass of gas and water:

$$T_i = \frac{T_g(t) * M_{th,g}(t) + T_w(t) * M_{th,w}(t)}{M_{th,g}(t) + M_{th,w}(t)} \tag{4.18}$$

where $T_g(t)$ and $T_w(t)$ are the temperature of gas and water as a function of time respectively in °C, and $M_{th,g}$, $M_{th,w}$ is thermal mass for gas and water respectively in J/K.

To, exterior temperature in °C. Calculated by using the measured bath temperature (cooling water), and an offset value. To is given by:

$$T_o = T_b(t) + offset \tag{4.19}$$

Where T_b is the bath temperature as a function of time. The offset value is calculated in two steps. The first step is to find the average of the initial 19 values for both Ti and Tb in the data

set. The second step is to subtract $Tb_{average}$ from the $Ti_{average}$. This difference is the margin of error in the temperature gauges.

Masses of water and hydrate are found quite similarly, where the moles of each component is known from previous calculations. A general equation shows the procedure:

$$m(kg) = M_{phase}\left(\frac{g}{mole}\right) * N_{phase}(t)(mole) * 0{,}001(\frac{kg}{g}) \tag{4.20}$$

where M is the molar weight, N is the amount of moles as a function of time, and 0,001 is simply a conversion from grams to kilograms as everything should be in SI-units.

The molar amount of gas, N_g, in moles is simply copied from previous calculations.

The final vector is the gas consumption rate in mole/s, which is also previously calculated; however, a minor modification is needed, which follows:

$$\dot{N}_g(t)\left(\frac{mole}{s}\right) = \dot{N}_g(t)\left(\frac{mole}{\min}\right) * \frac{1}{60}(\frac{min}{s}) \tag{4.21}$$

To summarize the vectors transferred to MatLab:

- Interior temperature, Ti [°C]
- Exterior temperature, To [°C]
- Mass of water, m_w [kg]
- Mass of hydrates, m_H [kg]
- Moles of gas, Ng [mole]
- Gas consumption rate, $\dot{N}_g$ [mole/s]

With the data from the excel spreadsheet completed, the preparation for the simulation could start. Values for the inner heat coefficient were calculated for 500, 700, and 1200 RPM, to see if the simulated data correlated to the calculated data using the theory of Ebrahimi et al. and equation (2.13). The constants were found by calculating for a 7°C case, and the only variable in the entire equation became the rotating speed.

Table 7 Constants for water at 7 °C

Water density, ρ	999	kg/m3
Diameter of cell, Dt	0.06	m
Diameter of mixer, Da	0.045	m
Thermal conductivity, K	0.58313	W/m·K
Specific heat capacity, Cp	4096	J/kg·K
Viscosity, μ	0.0013775	Pa·s
Pr-number	9.67578413	-

4.3 Simulation

With the needed data calculated, the simulation phase can take place. Before running any of the simulation scripts, sorting of the transferred data from the excel spreadsheet has to take place. This is completed by running the script, MAIN_vectorize, which vectorizes the array of pre-calculated time series collected from the spreadsheet. Configuring them in a way that makes it possible for MatLab to understand them.

After the data is optimized for MatLab, the simulation script MAIN_heat_trans_genT, is initialized. This script runs a radial heat transfer prediction, specifically designed for the titanium cell used in the experiments. The parameters needed for the script are the following:

- "Best guess" estimates of outer,-and inner heat coefficients
- Material properties for fluid, gas, and solid(titanium cell)
- Mass of water and hydrate in cell
- The molar amount of gas
- The gas consumption rate
- The measured interior temperature, and the outside temperature (cooling bath)

With these input parameters, the script simulates the temperature developments, as well as the predicted hydrate generation. Examples of the plots from the simulations are shown in Figure 14 and Figure 15:

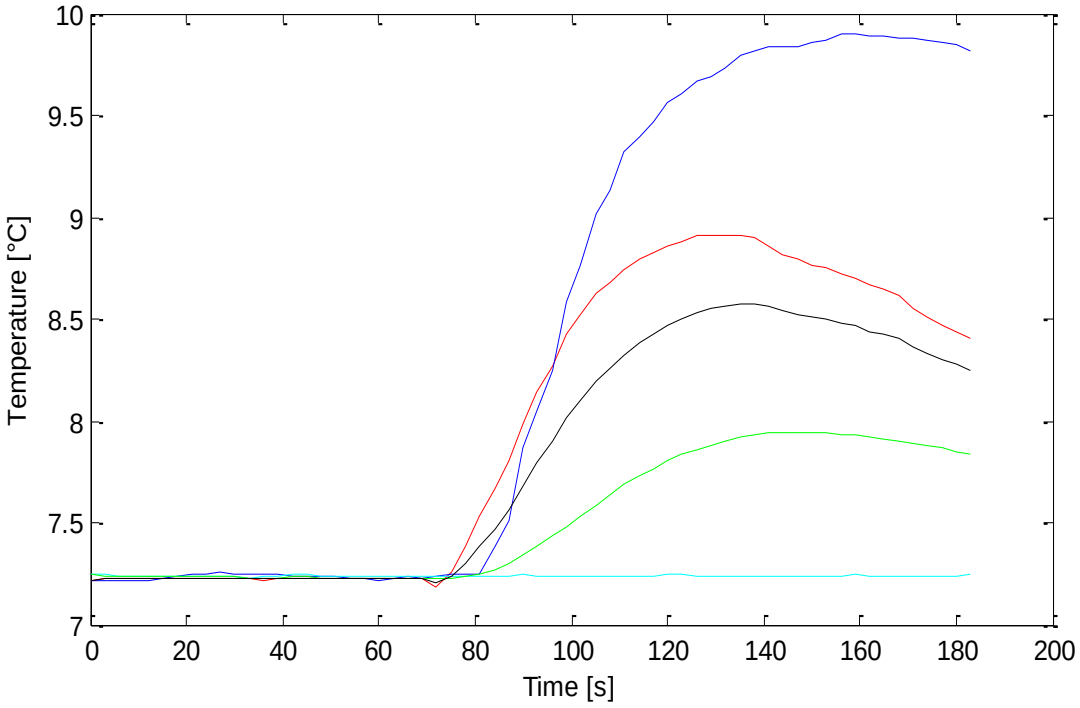

Figure 14 Measured, calculated and simulated temperatures. Red curve shows Simulated interior temperature, blue curve shows Measured interior temperature, black curve shows Calculated inner wall temperature, green curve shows Calculated outer wall temperature, cyan curve shows Measured bath temperature

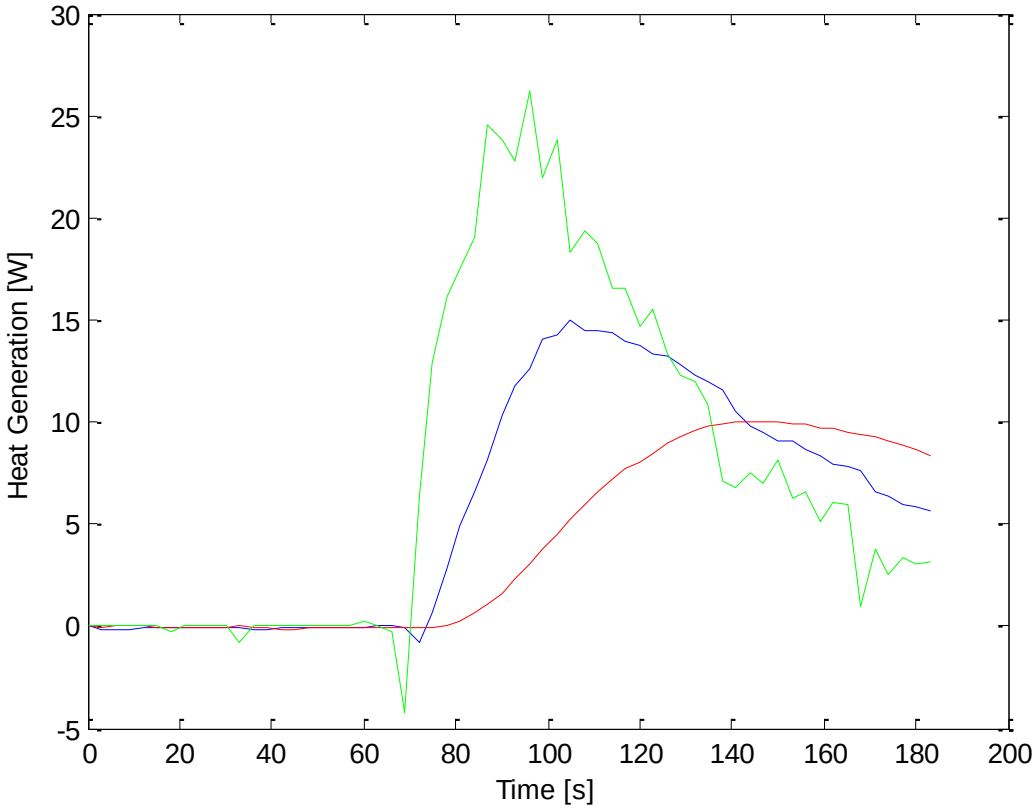

Figure 15 Simulated heat transfers. Green curve shows Simulated heat of hydrate generation, blue curve shows simulated heat to/from inner wall, red curve shows Simulated heat to/from outer wall.

As we can see from Figure 14 there is a rather large gap between the simulated (red curve) and measured (blue curve) temperatures, which arises because a fixed value for the inner heat coefficient is a "best guess" constant. Another script was implemented as a result, which was called MAIN_heat_trans_gold_simple. This script fixated on the inner heat coefficient, to find the value of h_i, which created the minimum deviation between simulated,-and measured interior temperature. A result of this script is shown in Figure 16 for a new simulation conducted on the same data set as used for Figure 14.

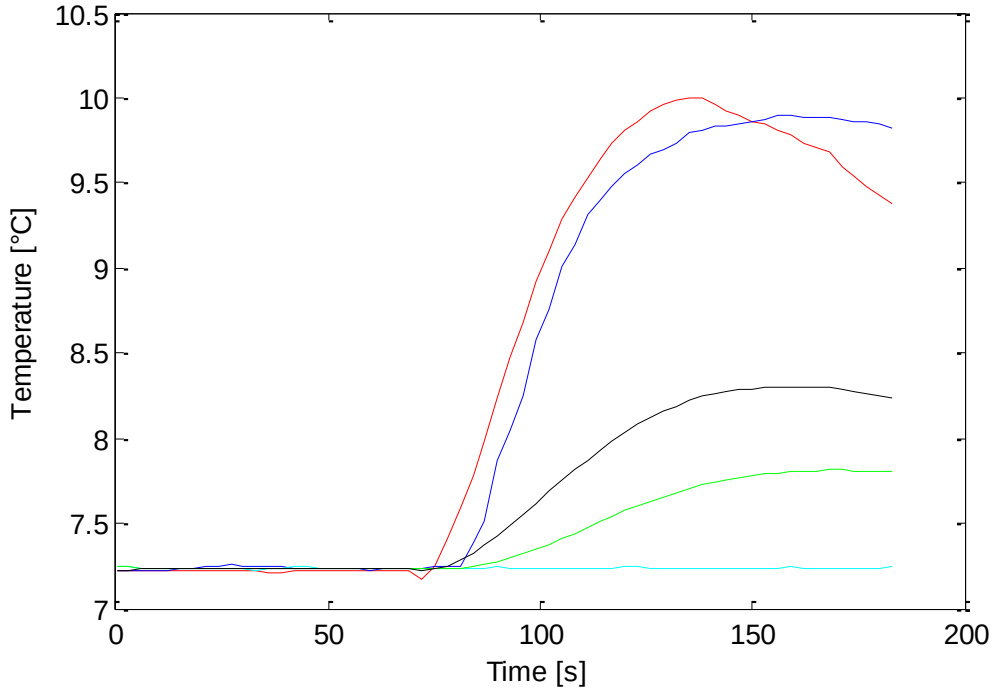

Figure 16 Plot after implementing "best fit" script. Red curve shows Simulated interior temperature, blue curve shows Measured interior temperature, black curve shows Calculated inner wall temperature, green curve shows Calculated outer wall temperature, cyan curve shows Measured bath temperature

A clear improvement is observed in Figure 16 where the simulated (red) follows the linear part of the measured (blue) with very little deviation compared to the original, Figure 14. The scripts used in this thesis are custom made by Professor Runar Bøe, specifically for this kind of simulation. The entire scripts can be seen in the appendix A2.

5 Results and discussion

A total of 53 simulations were completed, and as the simulation progressed, it was clear that by using the minimum deviation method for the inner heat coefficient, one could get a visually good curve, where simulated and measured inner temperature correlated well. However, the goal of the thesis was to test if the inner heat coefficient could be estimated for a specific, or even better, a general case within the corresponding region, which in this thesis was the early growth phase. This was done because the model itself gave good correlations between measured and simulated readings of the inner temperature, but the inner heat coefficient seemed arbitrary at best before running the best fit script.

In the upcoming chapter, the results of simulated inner heat coefficients, using the "best fit" script, are shown for temperature ranging from 6-8 °C, with varying water amounts, and for different rotational speeds. The experimental runs mentioned in the tables, is the marking of where the raw data is collected with respect to Nordbø's experiments (Nordbø, 2013). Tables 8-13 shows the results of the inner heat coefficient gained from the simulations.

Table 8 Simulation results for 6°C and 50 ml initial water

Rotation (rpm)	Experimental run	Simulated Hi
500	1	814
500	2	627
500	3	770
700	1	220
700	2	257
700	4	276
1200	1	234
1200	2	240
1200	4	274

Table 9 Simulation results for 6 °C and 100 ml initial water

Rotation (rpm)	Experimental run	Simulated Hi
500	1	1267
500	2	3186
500	3	1050
700	1	1357
700	2	1525
700	3	1045
1200	1	1054
1200	2	1232
1200	3	1283

Table 10 Simulation results for 7°C and 50 ml initial water

Rotation (rpm)	Experimental run	Simulated Hi
500	1	1439
500	2	937
500	3	945
700	1	443
700	2	443
700	3	460
1200	1	518
1200	2	540
1200	3	484

Table 11 Simulation results for 7°C and 100 ml initial water

Rotation (rpm)	Experimental run	Simulated Hi
500	1	1731
500	2	1402
500	3	453
500	4	1655
700	1	1595
700	2	1955
700	3	1751
1200	1	1437
1200	2	1556
1200	3	1527

Table 12 Simulation results for 8°C and 50 ml initial water

Rotation (rpm)	Experimental run	Simulated Hi
500	1	1201
500	2	1775
500	3	897
700	1	3004
700	2	100000
700	3	1207
1200	1	948
1200	2	1163
1200	3	900

Table 13 Simulation results for 8 °C and 100 ml initial water

Rotation (rpm)	Experimental run	Simulated Hi
500	1	1219
500	2	1185
500	3	921
700	2	1932
700	3	1534
1200	1	997
1200	2	1522

From table 8, we see the results of the hi-simulation from 6°C, 50 ml. The readings from the 700,-and 1200 rpm trials give very satisfactory correlations, especially the 1200-rpm region where there is little deviation. The 500-rpm readings are slightly more scattered.

Table 9 shows the results from 6°C and 100 ml initial water trials. Observing a similar trend as Table 8, with a decreasing hi-value for increasing stirring rates. However, the coherence of the values, seem to increase for the higher stirring rates.

Similar to Table 9, the values in the 500 rpm-region for Table 10 are slightly more incoherent than the counterparts of 700,-and 1200 rpm. With respect to the hi-values, the trend that was observed for the two previous tables, does not apply here. The largest hi-values can still be found in the 500-rpm region, but instead of a steady decline as a function of rotation speed, the hi-values for the 700 rpm-region drop to lower values than the 1200-rpm values. In terms of consistency, both 700,-and 1200 rpm continue to show good correlation.

In Table 11, it is observed, once again, that hi-values decrease as stirring rates increase. Furthermore, the 500-rpm readings still fluctuate more than the other stirring rates.

When viewing Table 12 the 700-rpm readings stand out, especially for experimental run one and two. Experimental run 1 gives a hi-value that looks particularly large compared to the other values obtained from the simulation. Experimental run two is a result of the simulation program failing to find a hi-value that yields little to no variance between simulated and measured internal temperature. The algorithm used in the simulation has a fixed maximum for the hi-values, which is 100000. This would mean that there was close to none heat resistance through the titanium cell, making the result dubious.

Table 13 shows the results for 8°C and 100 ml initial water. It is observed an opposite trend in terms of consistency compared to the majority of preceeding tables. The 500-rpm readings show the best correlation. In terms of decreasing hi-values as a function of increasing stirring rates, no clear-cut trend can be seen. The average of 700,-and 1200 rpm both surpass the 500-rpm readings, where 700-rpm exhibits the largest values.

Predictions around the inner heat transfer coefficient were also made by using the theory of Ebrahimi et al. where similar experiments were performed.

Table 14 Calculated values for 7°C

Rotation in rpm	Rotation in Hz (1/s)	Reynolds number	Hi
500	8.33	12233.30799	4166
700	11.67	17138.37985	5222
1200	20	29371.68784	7492

It became clear early on that the Hi-values from Table 14 exceed the general value range from the simulations. However, the margin of error may be accounted for, because the constant in equation (2.13) of 0.37 is a result of a regression, and accounts for the mixer geometries effect on the heat transfer. Knowing that the mixer-blade used in Therese Nordbø's experiments consist of a single rotating blade, instead of three bladed "propeller" which is used in Ebrahimi et al.'s experiments, the different shapes and geometries may account for the margin of error.

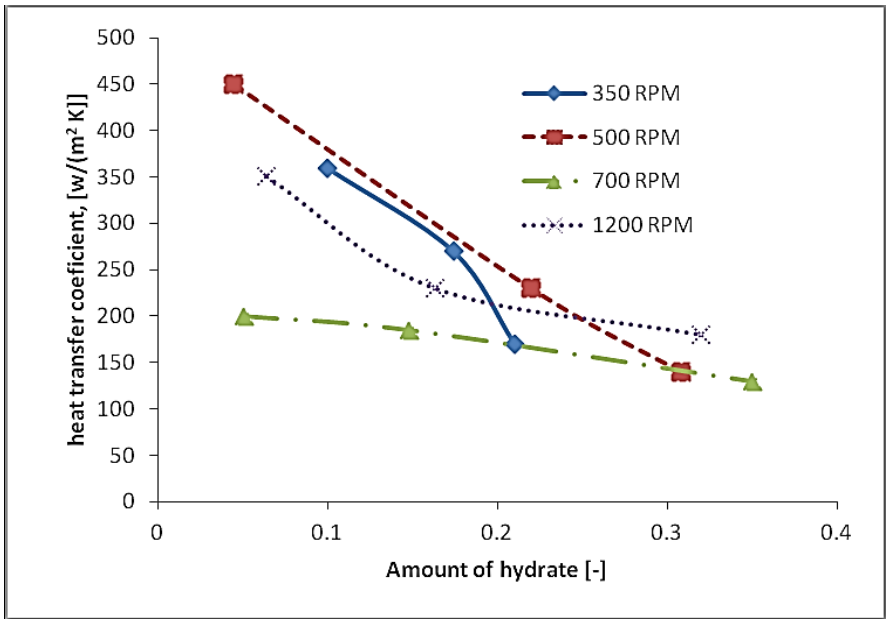

Figure 17 Heat transfer coefficient with different stirring rates as a function of hydrate growth (Linev'uks, 2014)

However, the prevalent was a declining inner heat coefficient, as a function of increasing stirring rate. This is in direct contrast to what Ebrahimi et al. proposed. Furthermore, the experiments by Ebrahimi et al. were completed in the absence of hydrate growth, which raises the question of the impact the hydrate phase, has on the heat coefficient, even at the early phase. Calculations conducted at UiS, by PhD candidate Mendinyo using data from Nataliya Linev'yuks experimental BSc work (2014) Figure 17, show a similar trend with decreasing Hi values by increasing stirring rate as observed through the present work. In addition, it is observed that the inner heat coefficient for 500-rpm is the largest, whilst the 1200-rpm is placed in between, and the 700-rpm has the lowest values. This is in agreement with the general trend of the results from this thesis, showing a steady decline of hi-value by increased stirring in the region between, 500 rpm, and 1200-rpm.

The rather large inner heat coefficient values obtained, which can be seen in Table 12 (700 RPM, experimental run 2), or Table 9 (500 RPM, experimental run 2) were unexpected as increased stirring should increase the heat transfer efficiency. This could however be remedied by modifying equation (4.19). Previously the offset value was calculated by the average of the first 19 values of Ti, and Tb (cooling bath), but after closer examination of the margin of error for the gauges used in the laboratory, a fixed value of 0.11 was deemed more accurate. This affects the relation between the stirring rate, and the simulated/estimated inner heat coefficient, as shown in Figure 18. Greater fluctuations appeared damped and the curve approached the form of a slow decaying, or an approximate linear relation.

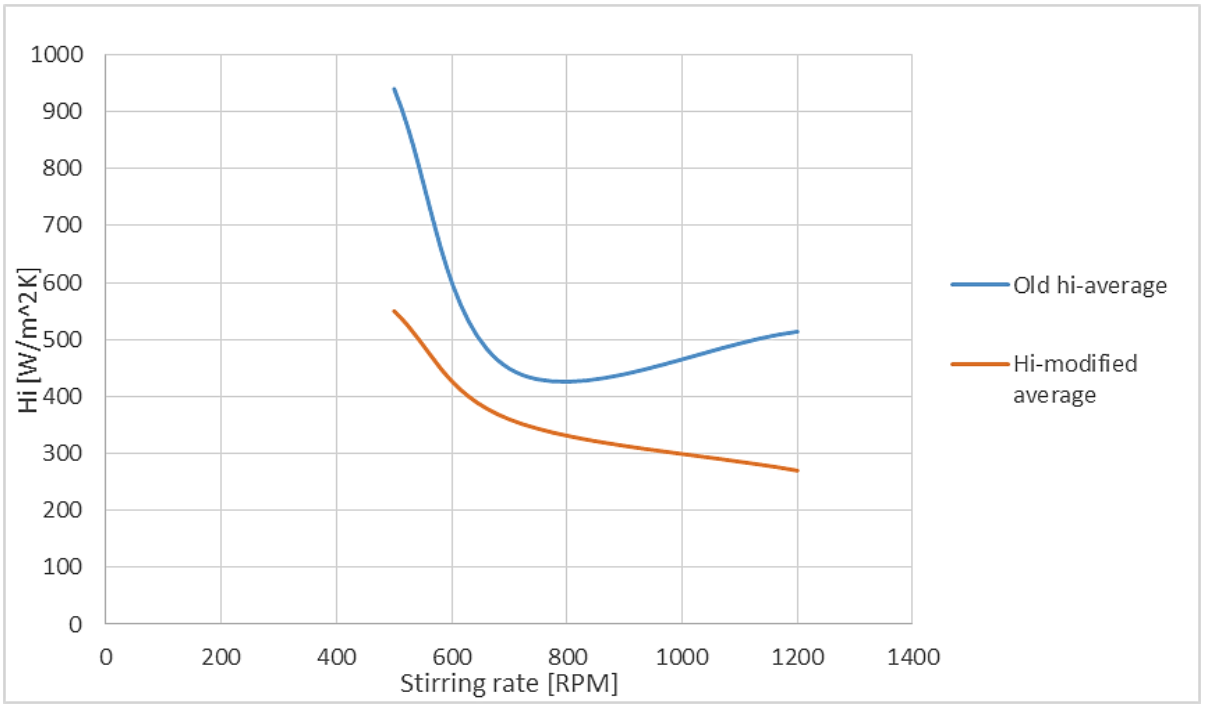

Figure 18 Comparison of hi-values, before and after modification

As seen in Figure 18, with the fixed value for the margin of error in the equipment, the values for *hi* are lowered, and the curve smoothens somewhat.

Another important factor with respect to the inner heat coefficient is the selection of raw data for the simulation. In the limited time-specter, which the simulation takes place, the selection affects the prediction of the inner heat coefficient considerably. The ideal start point of the selection is precisely where the hydrate growth is initiated by a rapid gas consumption increasing to values in the region 250 to approximately 500 Nml/min dependent on experimental conditions. Gas consumption as a function of time is illustrated in Figure 19. In addition, Figure 20 found in appendix A1, illustrates gas consumption and temperature profiles as a function of time. The start point, and the maximum flow point need to be included for proper simulation. However, for low stirring rates this can be difficult, because of a more progressive build-up of gas consumption. This selection can be a possible cause for values, which become very high, such as the case with 8°C, 50 ml, 700-rpm, experimental run two.

With the somewhat large inner heat coefficient values addressed, the focus shifts to the trends seen with increasing stirring rates vs decreasing hi-values. Possible causes are considered below:

1. Potential heat loss through the top lid was regarded negligible due to major contact with a gas phase with lower heat capacity than water, though some contact with water could be expected at the higher stirring rates. However, since ambient temperatures were above the experimental temperatures any heat *loss* could be ruled out, assuming heat absorption is more likely. With respect to heat absorbed, tests were conducted, and the effect was found to be negligible.
2. Looking at the different conversion rates of water into hydrate, and the gas consumption, for different stirring rates the following results were obtained for 7°C and 50 ml, by using modified offset value:

Table 15 Hydrate mass and water conversion as a function of stirring rate

Stirring rate [RPM]	Hydrate mass at end of trial[g]	Water converted [%]	Hi [W/m^2·K]
500	2.69	4.68	550
700	3.14	5.47	360
1200	3.63	6.30	270

The amount of water converted into hydrates is proportional with the amount of gas consumed. Figure 19 illustrates the relation between water converted, and stirring rate via cumulative gas flow versus time. This figure shows the water conversion ratio increases by increasing stirring rate. Increased amount of hydrate present would affect the heat transfer properties, most probably by a reduction as function of increased stirring rate.

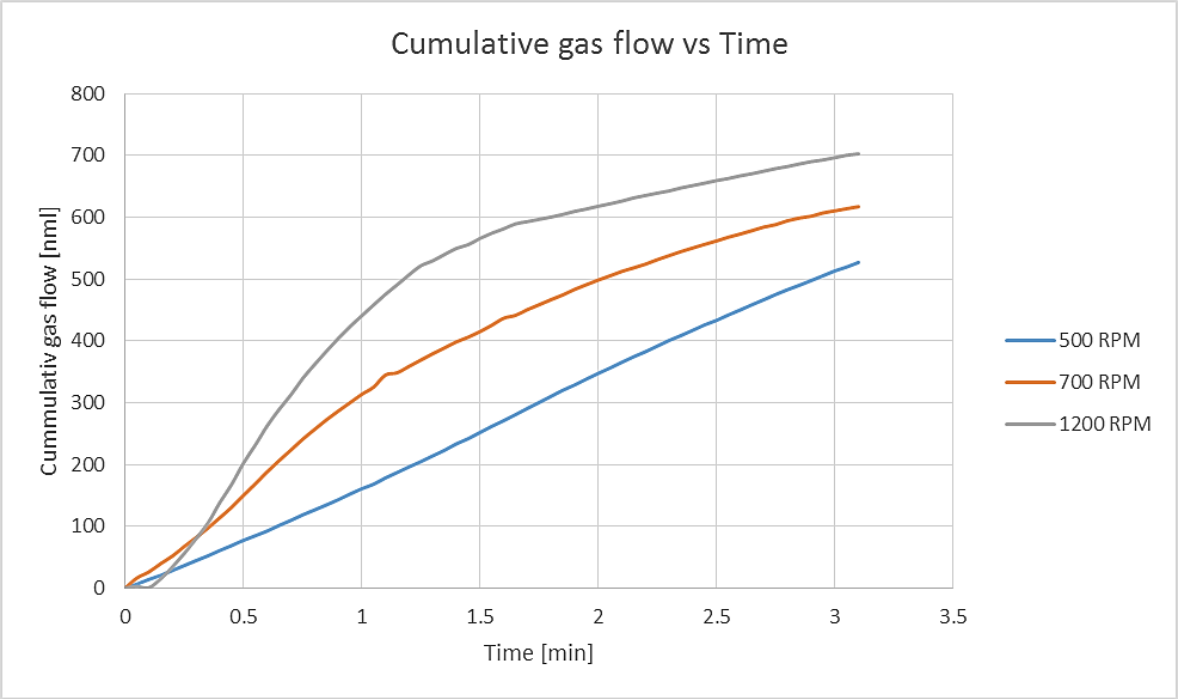

Figure 19 Cumulative gas flow as a function of stirring rate

The analysis of data shows that with increasing stirring rates, the amount of gas consumed increases. This in turn, leads to an increase of hydrates formed. When hydrates form, they change the environment, including the inner heat coefficient. Initially however, the effect of such small amounts of hydrates present was assumed to be insignificant. However, by not ruling out the effect it could serve as a possible explanation for observing the opposite trend of what was expected with respect to the effect of stirring rate on the inner heat coefficient. Without hydrates in the system, increased heat transfer by increased stirring would be expected.

As with any experiment, there are margins of error. Ideally when reproducing an experiment, the conditions should be the same. However, this can in practice be very difficult, as any interference or change can alter the outcome, and possibly result in greater differences between parallel experiments than anticipated. This is important to keep in mind when analyzing the results of the simulations. What are observed as comparatively large differences in Hi-values between stirring rates, could potentially be experimental margins of error.

The actual stirring effect is also an uncertainty, because the stirrer design is not ideal. The plane stirrer blade will create rotation of the liquid inside with less turbulence than would be created by a more efficient stirrer system commonly used in reactors. Especially during low stirring rates, there is a real concern regarding turbulence, where the surrounding body of water may rather flow alongside the blades, which effectively negates the wanted turbulence effect. The stirring efficiency plays a large role in determining the limiting factor of the process, as high stirring efficiency ensures good heat convection in the fluid. In the test cells, it is likely that the stirring efficiency is not good enough to create pure heat transfers as the only limiting factor, which leads to mass transfer as a contributing factor as well. Another problem with a batch type reactor used in the present study is the simultaneous effect of increasing amount of hydrates in the liquid phase as a function of increased stirring rate. A continuous process reactor design with balanced removal of produced hydrates, and supply of fresh water could help eliminate unknown effects related to the hydrate concentration in the reactor.

6 Conclusions

In conclusion, the following key points are summarized:

1. When predicting a value-range for the inner heat coefficients, the results were satisfactory for most cases. The overall consistency for each case (similar temperature, initial water, stirring rate), provided a good basis for assuming a reasonable range for the inner heat coefficient.
2. The inner heat coefficient seems to decrease as a function of increased stirring rates. This finding was reinforced by investigating the raw data, and looking at the gas consumption, which increases as stirring rates increase. If the gas consumption increases, it is a reasonable assumption that the amount of hydrate formation increases as well. This was confirmed by the raw data, and correlated well with the simulated inner heat coefficient.
3. The offset value discussed in chapter 5, and found in equation (4.19) should be adjusted to 0.11 and implemented in the simulation program as a fixed value. This is in better agreement when considering the delay/margin of error of the gauges in the experimental equipment, and also renders TO-values (vector transferred to MatLab), which are more consistent with what is observed at the temperature gauges in the laboratory.
4. The original relationship between stirring rate, and the inner heat coefficient, described in equation (2.13), and in Table 15, is concluded to be of little relevance as a stand-alone prediction of the inner heat coefficient with regard to hydrate growth. This is due to the impact the phase change apparently has on the viscosity, which in turn alters the Reynolds number.
5. If the stirring design does not supply needed effect for heat transfer to become the only limiting transfer, mass transfer should also be included in the model, to avoid miscalculations.

7 Future work

For future work, it would be interesting to see an empirical analysis of the inner heat coefficient as a function of increasing hydrate content in a test cell. This to see if there are any clear trends, i.e. if the inner heat coefficient can be described and estimated graphically. In addition, it could be studied if there are any major differences by altering the test temperature, or initial water amount.

The simulations carried out as a part of this thesis were based on three to four experiments under the same conditions. It could be beneficial to run more experiments for each case, as the experimental runs will always vary to a certain extent. With a higher number of experiments, higher accuracy can be achieved in stipulating which values for the inner heat coefficient are under,-or overestimated compared to the others, and pinpointing *why* they differ from the rest.

8 References

(2004). Charting the Future of Methane Hydrate Research in the United States [Picture], The National Academies Press.

Anderson, G. K. (2004). "Enthalpy of dissociation and hydration number of methane hydrate from the Clapeyron equation." Journal of Chemical Thermodynamics **36**(12): 1119-1127.

Buanes, T., et al. (2006). "Computer simulation of CO2 hydrate growth." Journal of crystal growth **287**(2): 491-494.

Bøe, R. (2014) Personal communication

Davy, H. (1811). "The Bakerian Lecture. On some of the Combinations of Oxymuriatic Gas and Oxygene, and on the chemical Relations of these Principles, to inflammable Bodies." Philosophical Transactions. Ser. B **101**(1): 1-7.

Ebrahimi, A., et al. (2009). "Effect of Mixer Rotational Speed on Heat Transfer Coefficient in Preparation of Nickle Perovskite From Laboratory to Bench Scale." Iranian Journal of Chemical Engineering **6**(3).

Englezos, P., et al. (1987). "Kinetics of formation of methane and ethane gas hydrates." Chemical Engineering Science **42**(11): 2647-2658.

Englezos, P., et al. (1987). "Kinetics of gas hydrate formation from mixtures of methane and ethane." Chemical Engineering Science **42**(11): 2659-2666.

Freer, E. M., et al. (2001). "Methane hydrate film growth kinetics." Fluid Phase Equilibria **185**(1–2): 65-75.

Fukumoto, K., et al. (2001). "Hydrate formation using water spraying in a hydrophobic gas: A preliminary study." AIChE Journal **47**(8): 1899-1904.

Gupta, A., et al. (2008). "Measurements of methane hydrate heat of dissociation using high pressure differential scanning calorimetry." Chemical Engineering Science **63**(24): 5848-5853.

Hammerschmidt, E. G. (1934). "Formation of Gas Hydrates in Natural Gas Transmission Lines." Ind. Eng. Chem. **26**: 851-855.

Hirai, S. and H. Sanda (2004). "Growth-controlling processes of CO2 gas hydrates." American Mineralogist **89**(8-9): 1260-1263.

Incropera, F. P. and D. P. DeWitt (1996). Fundamentals of heat and mass transfer, Wiley.

Ito, Y., et al. (2003). "Microscopic observations of clathrate-hydrate films formed at liquid/liquid interfaces. II. Film thickness in steady-water flow." Chemical Engineering Science **58**(1): 107-114.

Kashchiev, D. and A. Firoozabadi (2002). "Nucleation of gas hydrates." Journal of crystal growth **243**(3): 476-489.

Lievois, J. S. (1987). Development of an automated, high pressure heat flux calorimeter and its application to measure the heat of dissociation of methane hydrate, Rice University. **PhD:** 162.

Linev'yuk, N. (2014). "Experimental Study of Hydrate Growth Kinetics". BSc Thesis, Department of Petroleum Engineering, University of Stavanger, p 34 – 42.

Lirio, C. F. S. and F. L. P. Pessoa (2013). "Enthalpy of dissociation of simple and mixed carbon dioxide clathrate hydrate." Chemical Engineering Transactions **32**: 577-582.

Maini, B. B. and P. R. Bishnoi (1981). "Experimental investigation of hydrate formation behaviour of a natural gas bubble in a simulated deep sea environment." Chemical Engineering Science **36**(1): 183-189.

Malegaonkar, M. B., et al. (1997). "Kinetics of carbon dioxide and methane hydrate formation." The Canadian Journal of Chemical Engineering **75**(6): 1090-1099.

McMullan, R.K., Jeffrey, G.A., J. Chem. Phys., 42, 2725 (1965).

Mochizuki, T. and Y. H. Mori (2005). Clathrate-hydrate Film Growth Along Water/hydrateformer Phase Boundaries - A Conductive Heat-transfer Model. Fifth Int. Conference on Gas Hydrates. Trondheim.

Mochizuki, T. and Y. H. Mori (2006). "Clathrate-hydrate film growth along water/hydrate-former phase boundaries—numerical heat-transfer study." Journal of crystal growth **290**(2): 642-652.

Mori, Y. H. (2001). "Estimating the thickness of hydrate films from their lateral growth rates: application of a simplified heat transfer model." Journal of crystal growth **223**(1–2): 206-212.

Moudrakovski, I. L., et al. (2004). "Methane and Carbon Dioxide Hydrate Formation in Water Droplets: Spatially Resolved Measurements from Magnetic Resonance Microimaging." The Journal of Physical Chemistry B **108**(45): 17591-17595.

Nerheim, A. R., et al. (1994). Investigation Of Hydrate Kinetics In The Nucleation And Early Growth Phase By Laser Light Scattering, International Society of Offshore and Polar Engineers.

Nordbø, T. (2014). "Hydrate growth kinetics: A study on the relation between energy release rates and gas consumption during methane hydrate formation and growth". MSc Thesis, Department of Petroleum Engineering, University of Stavanger.

Ohmura, R., et al. (2000). "Measurements of clathrate-hydrate film thickness using laser interferometry." Journal of crystal growth **218**(2–4): 372-380.

Ohmura, R., et al. (2003). "Statistical Study of Clathrate-Hydrate Nucleation in a Water/Hydrochlorofluorocarbon System: Search for the Nature of the "Memory Effect"." The Journal of Physical Chemistry B **107**(22): 5289-5293.

Ohmura, R., et al. (1999). "Formation, growth and dissociation of clathrate hydrate crystals in liquid water in contact with a hydrophobic hydrate-forming liquid." Journal of crystal growth **196**(1): 164-173.

Radhakrishnan, R. and B. L. Trout (2002). "A new approach for studying nucleation phenomena using molecular simulations: Application to CO2 hydrate clathrates." The Journal of Chemical Physics **117**(4): 1786-1796.

Salamatin, A. N., et al. (1998). "Post-nucleation conversion of an air bubble to clathrate air–hydrate crystal in ice." Journal of crystal growth **193**(1–2): 197-218.

Servio, P. and P. Englezos (2003). "Morphology of methane and carbon dioxide hydrates formed from water droplets." AIChE Journal **49**(1): 269-276.

Servio, P. and P. Englezos (2003). "Morphology study of structure H hydrate formation from water droplets." Crystal growth & design **3**(1): 61-66.

Shi, B.-H., et al. (2011). "An inward and outward natural gas hydrates growth shell model considering intrinsic kinetics, mass and heat transfer." Chemical Engineering Journal **171**(3): 1308-1316.

Shindo, Y., et al. (1993). "Kinetics and mechanism of the formation of CO2 hydrate." International Journal of Chemical Kinetics **25**(9): 777-782.

Skovborg, P. and P. Rasmussen (1994). "A mass transport limited model for the growth of methane and ethane gas hydrates." Chemical Engineering Science **49**(8): 1131-1143.

Sloan, E. D. and C. A. Koh (2008). Clathrate Hydrates of Natural Gases. Boca Raton, CRC Press : Taylor & Francis Group.

Smith, J. M., et al. (2005). Introduction to chemical engineering thermodynamics. Boston, McGraw-Hill.

Stackelberg, M. and H. R. Muller (1954a). "Feste Gashydrate. II - Struktur und Raumchemie." Z. Electrochemie **58**: 25-39.

Stackelberg, M. and H. R. Muller (1954b). "On the Structure of Gas Hydrates." 1319-1320

Sugaya, M. and Y. H. Mori (1996). "Behavior of clathrate hydrate formation at the boundary of liquid water and a fluorocarbon in liquid or vapor state." Chemical Engineering Science **51**(13): 3505-3517.

Svartås, T.M. (2014). Personal communication.

Svandal, A., et al. (2005). "The influence of diffusion on hydrate growth." Journal of Phase Equilibria and Diffusion **26**(5): 534-538.

Taylor, C. J. (2006). Adhesion force between Hydrate Particles and Macroscopic Inverstigations of Hydrate film Growth at the Hydrocarbon/Water interface. Chemical Engineering. Golden, Colorado, Colorado School of Mines. **MSc**.

Taylor, C. J., et al. (2007). "Macroscopic investigation of hydrate film growth at the hydrocarbon/water interface." Chemical Engineering Science **62**(23): 6524-6533.

Uchida, T., et al. (1999). "Microscopic observations of formation processes of clathrate-hydrate films at an interface between water and carbon dioxide." Journal of crystal growth **204**(3): 348-356.

Uchida, T., et al. (2002). "CO2 hydrate film formation at the boundary between CO2 and water: effects of temperature, pressure and additives on the formation rate." Journal of crystal growth **237–239, Part 1**(0): 383-387.

Wyslouzil, B. E., et al. (1997). "Small Angle Neutron Scattering from Nanodroplet Aerosols." Physical Review Letters **79**(3): 431-434.

Appendix

Included the following appendix are plots of gas consumption and temperature profiles during incipent hydrate growth, and matlab codes for each script used in the simulation.

Appendix A1: Gas consumption – temperature profile during incipient hydrate growth

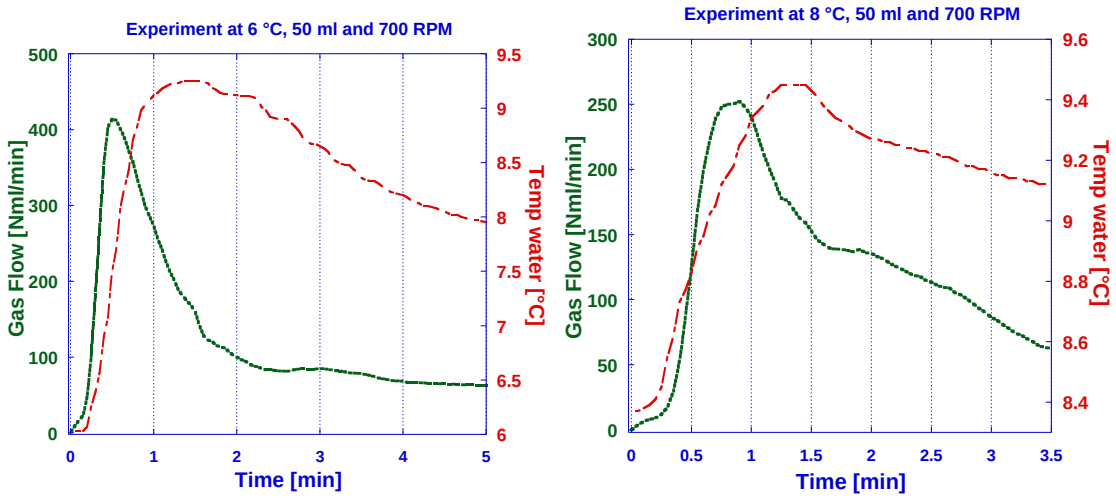

Figure 20 Graphs showing gas consumption (gas flow, green) and temperature (red) in water phase during the first 5 minutes of hydrate growth at 6 and 8 °C temperature in cooling bath

Appendix A2: MatLab codes used in scripts

MAIN_vectorize is given by:

```
%%%%%%%%%%%%%%%%%%%%%%%%%%%%%%%%%%%%%%%%%%%%%%%%%%%%%%%%%%%%%%%%%%%%%%%%%%%%%%%
% Script to vectorize the array of precalculated time series from the early
% stage analysis spreadsheet. Copy an array of the 6 horizontal vectors
% TIr [C]   TO [C]  mw[kg]  mH[kg]  Ng [mole]   dNR/dt [mole/s] in 1 go,
% and then tranfer them to single ones.

global TO TIr mw mH Ng dNRdt

TIr     = [];
TO      = [];
mw      = [];
mH      = [];
Ng      = [];
dNRdt   = [];

TIr     = A_pastespecial(:,1);
TO      = A_pastespecial(:,2);
mw      = A_pastespecial(:,3);
mH      = A_pastespecial(:,4);
Ng      = A_pastespecial(:,5);
dNRdt   = A_pastespecial(:,6);
```

MAIN_heat_trans_genT is given by:

```
%%%%%%%%%%% REQUIRED VECTORS AND THEIR UNITS %%%%%%%%%%%%%%%%%%%%%%%%%
%TO     [C]             Representative cooling water temp.
%TIr    [C]             Representative internal temperature (measured)
%mw     [kg]            Mass of water in cell
%mH     [kg]            Mass of hydrate in cell
%Ng     [mole]          Moles of gas in cell
%dNRdt  [mole/s]        Methane consumption rate in forming hydrate

% This verison calculates the internal cell temperature based on a heat
% balance controlled by the externally estimated methane consumption rate
% multiplied with a tabulated value for the enthalpy of generation, and the
% convection heat controlled by the inner heat transfer coefficient

% Constants:
% Titanuim:
k   = 21.9;  % W/m K
rho = 4506;  % kg/m3
c   = 544;   % J/kg K
% Cylinder:
% Small cell
Ri      = 0.03;  % m
```

```
Ro      = 0.045; % m
% Large cell
%Ri      = 0.045; % m
%Ro      = 0.06;  % m
% Heigth is the same for both cells
delta   = 0.05;  % m
% Fluids:
% mw      = 0.05; % kg (mass of water now obtained from materials account)
% Specific heats:
cw      = 4200;     % J/kg K (water)
Cpg     = 49.26;    % J/mole K (given by SRK at T = 8.14 C, p = 90.42 bar)
cH      = 2200;     % J/kg K (hydrate, sort of "average" from diff.
sources)
% Heat of generation for methane hydrate (average value)
Hgen    = 54000; % J/mole
% Cancel Ng for time varying gas content
% Ng      = 0.426;  % mole

% Heat transfer coefficients:
hO      = 1000  % W/m2 K
hI      = 362% W/m2 K
% Grid:
N   = 18;
Dt  = 3;    % s
% Calculated properties:
alpha   = k/(rho*c);
Dr      = (Ro - Ri)/N;
Fo      = alpha*Dt/Dr^2;
BiI     = hI*Dr/k;
BiO     = hO*Dr/k;
% CI needs recalculation for each time step in case of time varying ratio
% between the fluid phases (This value is initial value)
% CI      = 2*hI*pi*delta*Ri*Dt/(mw*cw + Ng*Cpg)
CI      = 2*hI*pi*delta*Ri*Dt/(mw(1,1)*cw + mH(1,1)*cH + Ng(1,1)*Cpg);
% XI needs recalculation for each time step. It's initieal value is by
% definition zero (growth hasn't started yet):
XI      = 0;
% Areas for heat rate calculations:
A_half  = 2*pi*(Ri + Dr/2)*delta;
A_nhalf = 2*pi*(Ro - Dr/2)*delta;
% Time steps in current border vector:
s       = size(TO);
s(:,2)  = [];
M   = s
% R-vector for plotting (R = 0 for interior of cell)
%R       = [];
%R(1,1)  = 0;
%for i   = 2:(N+2)
%    R(i,1)   = Ri + (i-2)*Dr;
%end


%Setting up the A-matrix for hydrate generation
%(This is ALMOST constant throughout, so this is an initialization):
A   = [];
% First row; entry I - cell interior:
```

```
A(1,1)  = (1 + CI);
A(1,2)  = -CI;
for j   = 3:(N+2)
    A(1,j)  = 0;
end
% Second row; entry 0 - inner border/wall:
A(2,1)  = -2*BiI*Fo;
A(2,2)  = (1 + 2*(BiI + (Dr/(2*Ri) + 1))*Fo);
A(2,3)  = -2*(Dr/(2*Ri) + 1)*Fo;
for j   = 4:(N+2)
    A(2,j)  = 0;
end
% Internal node rows 1 - (n-1) => i = 3 - (N+1):
for i   = 3:(N+1)
    for j   = 1:(i-2)
        A(i,j)  = 0;
    end
    r   = Ri + (i-2)*Dr;
    A(i,(i-1))  = (Dr/(2*r) - 1)*Fo;
    A(i,i)      = (1 + 2*Fo);
    A(i,(i+1))  = -(Dr/(2*r) + 1)*Fo;
    for j   = (i+2):(N+1)
        A(i,j)  = 0;
    end
end
% Last row; entry N+2 - outer border:
for j   = 1:N
    A((N+2),j)  = 0;
end
A((N+2),(N+1))  = 2*(Dr/(2*Ro) - 1)*Fo;
A((N+2),(N+2))  = (1 + 2*(BiO - (Dr/(2*Ro) - 1))*Fo);
%Inverting the A-matrix: (This must be moved inside the loop in case of
%time varyig gas content)
% AI  = inv(A);

% Initializing the Y-vector:
Y   = [];
% Cell internal:
Y(1,1)  = XI + TIr(1,1);
% Inner wall:
Y(2,1)  = TIr(1,1);
for i   = 3:9
    Y(i,1)  = TIr(1,1);
end
for i   = 10:(N+1)
    Y(i,1)  = TO(1,1);
end
Y((N+2), 1) = TO(1,1) + 2*BiO*Fo*TO(2,1);
%Y
%pause;
% Vectors for time series plotting:
Time    = [];
TI      = [];   % Interior; simulated
TIp     = [];   % Interior; measured, and copied over to get same dim.
TOp     = [];   % Need an extra plotting vector for the bath temperature
                %(to be of the same length as the time vector)
```

```
TWI     = [];   % Need to plot the wall temperatures too, sometimes
TWO     = [];   % TWI = inner wall, TWO = outer wall
%XI      = [];   % Group posing as temperature, from which the heat of
                 % hydrate generation is to be derived from
%HI      = [];   % Inner heat transfer coefficient (calc. or par.)

QI      = [];   % Heat to/from the interior
QO      = [];   % Heat to/from the cooling mantle
QR      = [];   % Heat of hydrate generation
% Starting time loop (With measured values the number of repetitions is
% given by the size of the input vectors, M):
t   = 0;
Time    = [Time; t];
TI      = [TI; TIr(1,1)];
TIp     = [TIp; TIr(1,1)];
TOp     = [TOp; TO(1,1)];
TWI     = [TWI; TIr(1,1)]; % Estimat
TWO     = [TWO; TO(1,1)]; % Estimat
%XI      = [XI; 0];
%HI      = [HI; hI];
% Initially, no heat when temperature is homogeneous (TI = TO), and no
% hydrate is yet formed.
QI      = [QI; 0];
QO      = [QO; 0];
QR      = [QR; 0];

for i   = 1:(M-2)
    % Inverting matrix:
    AI  = inv(A);
    % Calculate T-vector:
    T   = AI*Y;
    % Filling vectors for plotting and result export
    %XI  = [XI; T(1,1)];
    TI  = [TI; T(1,1)];
    TWI  = [TWI; T(2,1)];
    TWO  = [TWO; T((N+2),1)];
    TIp = [TIp; TIr((i+1),1)];
    TOp = [TOp; TO((i+1),1)];
    %HI  = [HI; hI];
    qI  =  -k*A_half*(T(3,1) - T(2,1))/Dr;
    QI  = [QI; qI];
    qO  = -k*A_nhalf*(T(N+2) - T(N+1))/Dr;
    QO  = [QO; qO];
    % calculating qR and updating XI for the time step:
    qR  = dNRdt((i+1),1)*Hgen;
    QR  = [QR; qR];
    XI  = qR*Dt/(mw((i+1),1)*cw + mH((i+1),1)*cH + Ng((i+1),1)*Cpg);
    % Updating CI:
    CI  = 2*hI*pi*delta*Ri*Dt/(mw((i+1),1)*cw + mH((i+1),1)*cH + ...
        Ng((i+1),1)*Cpg);
    % Updating Y-vector:
    Y   = T;
    Y(1,1)       = XI + T(1,1);
    %Y(2,1)       = T(2,1) + 2*BiI*Fo*TIr((i+2),1);
    Y((N+2), 1) = T((N+2),1) + 2*BiO*Fo*TO((i+2),1);
    % Updating A- matrix:
```

```
    A(1,1)      = 1 + CI;
    A(1,2)      = -CI;
    %Y
    %pause;
    t   = t + Dt;
    Time    = [Time; t];
end
t

% Vector for exporting time, TIp and TI:
ResT    = [];
ResT    = [Time, TIp, TI];

% Plotting resulting time series to screen

figure(3);
plot(Time, TI, 'r');
hold;
plot(Time, TIp);
plot(Time, TOp, 'c');
plot(Time, TWO, 'g');
plot(Time, TWI, 'y');
hold;

disp(' ');
disp('Figure 2');
disp('Red:          Simulated interior temperature');
disp('Blue:         Measured interior temperature');
disp('Yellow:       Calculated inner wall temperature');
disp('Green:        Calculated outer wall temperature');
disp('Light blue:   Measured bath temperature');



% Figure 4 = heat rate plots
figure(4);
plot(Time, QI);      % Blå - inner
hold;
plot(Time, QO, 'r');    % Rød - outer
plot(Time, QR, 'g');   % Grønn - hydratgenerering
hold;

disp(' ');
disp('Figure 4');
disp('Red:          Simulated heat to/from outer wall');
disp('Blue:         Simulated heat to/from inner wall');
disp('Green:        Simulated heat of hydrate generation');
```

MAIN_heat_trans_gold_simple is given by:

```
%%%%%%%%%%%%%%%%%%%%%%%%%%%%%%%%%%%%%%%%%%%%%%%%%%%%%%%%%%%%%%%%%%%%%%%%%%%%
% Finding the value for hI that minimizes the variance between measured and
% simulated temperature response for a given value (best guess /
% correllation) of hO (hO to be supplied by input or hard coded)



%%%%%%%%%%% REQUIRED VECTORS AND THEIR UNITS %%%%%%%%%%%%%%%%%%%%%%%%%%%%%%%
%TIr    [C]
%TO     [C]
%mw     [kg]
%mH     [kg]
%Ng     [mole]
%dNRdt  [mole/s]
%Either copy to workspace one by one, or transfer the whole array and run
%the independent script "MAIN_vectorize"

global TO TIr mw mH Ng dNRdt

%hO  = input('Outer heat transfer coefficient, [W/m2 K]: ');
hO   = 1000;


% hI expected to fall between the values A and B
A   = 50;  %W/m2K
B   = 100000;

R   = (sqrt(5) -1)/2;

% Initialize:
x   = A + R*(B - A);
u   = heat_trans_genT_f(x, hO);
y   = A + R^2*(B - A);
v   = heat_trans_genT_f(y, hO);
% Testing:
conv    = 1e-5;
while abs(x - y) >= conv
    if u > v
        B   = x;
        x   = y;
        u   = v;
        y   = A + R^2*(B - A);
        v   = heat_trans_genT_f(y, hO);
    else
        A   = y;
        y   = x;
        v   = u;
        x   = A + R*(B - A);
        u   = heat_trans_genT_f(x, hO);
    end
end
hI  = x
```